



**HAL**  
open science

## The 2018-ongoing Mayotte submarine eruption: Magma migration imaged by petrological monitoring

Carole Berthod, Etienne Médard, Patrick Bachèlery, Lucia Gurioli, Andrea Di Muro, Aline Peltier, Jean-Christophe Komorowski, Mhammed Benbakkar, Jean-Luc Devidal, Jessica Langlade, et al.

### ► To cite this version:

Carole Berthod, Etienne Médard, Patrick Bachèlery, Lucia Gurioli, Andrea Di Muro, et al.. The 2018-ongoing Mayotte submarine eruption: Magma migration imaged by petrological monitoring. *Earth and Planetary Science Letters*, 2021, 571, pp.117085. 10.1016/j.epsl.2021.117085 . hal-03353428

**HAL Id: hal-03353428**

**<https://uca.hal.science/hal-03353428v1>**

Submitted on 24 Sep 2021

**HAL** is a multi-disciplinary open access archive for the deposit and dissemination of scientific research documents, whether they are published or not. The documents may come from teaching and research institutions in France or abroad, or from public or private research centers.

L'archive ouverte pluridisciplinaire **HAL**, est destinée au dépôt et à la diffusion de documents scientifiques de niveau recherche, publiés ou non, émanant des établissements d'enseignement et de recherche français ou étrangers, des laboratoires publics ou privés.



Distributed under a Creative Commons Attribution 4.0 International License



22

23

24 **Highlights**

25

26 - Lavas erupted offshore Mayotte since May 2018 are evolved basanites (~5 wt% MgO).

27 - The eruption is fed by a deep (> 37 km) mantle reservoir.

28 - Primitive magma has undergone at least 50% of crystallization in a  $\geq 10 \text{ km}^3$  mantle  
29 reservoir.

30 - Magma transfer rate show that the eruption is steadily supplied from the deep mantle  
31 reservoir.

32 - After May 2019, ascending magma intersected a more evolved and shallower magma  
33 reservoir.

34

35 **Keywords:** Mayotte, submarine eruption, dredges, petrological model, mantle reservoirs,  
36 multiple storage zone

37

38

39

40

41

42

43 **Abstract**

44

45         Deep-sea submarine eruptions are the least known type of volcanic activity, due to the  
46 difficulty of detecting, monitoring, and sampling them. Following an intense seismic crisis in  
47 May 2018, a large submarine effusive eruption offshore the island of Mayotte (Indian Ocean)  
48 has extruded at least 6.5 km<sup>3</sup> of magma to date, making it the largest monitored submarine  
49 eruption as well as the largest effusive eruption on Earth since Iceland's 1783 Laki eruption.  
50 This volcano is located along a WNW-ESE volcanic ridge, extending from the island of Petite  
51 Terre (east side of Mayotte) to about 3,500 m of water depth. We present a detailed petrological  
52 and geochemical description of the erupted lavas sampled by the MAYOBS 1, 2, and 4 cruises  
53 between May and July 2019 and use these to infer characteristics and changes through time for  
54 the whole magmatic system and its dynamics from the source to the surface. These cruises  
55 provide an exceptional time-series of bathymetric, textural, petrological, and geochemical data  
56 for the 2018-2019 eruptive period, and hence bring an invaluable opportunity to better constrain  
57 the evolution of magma storage and transfer processes during a long-lived submarine eruption.  
58 Integrating the petrological signatures of dredged lavas with geophysical data, we show that the  
59 crystal-poor and gas-rich evolved basanitic magma was stored at mantle depth (> 37 km) in a  
60 large ( $\geq 10$  km<sup>3</sup>) reservoir and that the eruption was tectonically triggered. As the eruption  
61 proceeded, a decrease in ascent rate and/or a pathway change resulted in the incorporation of  
62 preexisting differentiated magma stored at a shallower level. Magma transfer from the deep  
63 mantle reservoir is syn-eruptive, as indicated by transfer times estimated from diffusion in  
64 zoned olivine crystals that are much shorter than the total eruption duration. Our petrological  
65 model has important hazard implications concerning the rapid and stealthy awakening of a deep  
66 gas-rich magma reservoirs that can produce unusually high output rates and long-lived eruption.



67 Sudden tapping of large crystal poor reservoirs may be the trigger mechanism for other rarely  
68 witnessed high-volume ( $> 1 \text{ km}^3$ ) effusive events.

69

## 70 **1. INTRODUCTION**

71

72 The discovery in May 2019 of an active volcanic submarine edifice of exceptional size 50  
73 km east of Mayotte island (Comoros Archipelago, Mozambique Channel, Fig. 1a) caused an  
74 immediate mobilization of the French scientific community (Feuillet et al., 2019), and the  
75 creation of the Mayotte Volcanological and Seismological Monitoring Network (ReVoSiMa,  
76 2021). The eruptive site is located on the distal part of a 60 km long WNW-ESE volcanic ridge  
77 that runs off the eastern flank of Mayotte, the subaerial expression of which is Petite Terre  
78 Island (Fig. 1b). As of October 2020, this volcano had risen 820 m above the 3300 m deep  
79 seafloor with an erupted lava volume of  $\sim 6.5 \text{ km}^3$  (ReVoSiMa, 2021). This volume implies  
80 exceptionally high time-averaged magma discharge rates ranging from 150 – 200  $\text{m}^3/\text{s}$  (first  
81 year), decreasing through 70 – 80  $\text{m}^3/\text{s}$  (May–July 2019) to less than 35 – 45  $\text{m}^3/\text{s}$  since August  
82 2019 (ReVoSiMa, 2021). As such, it represents by far the largest monitored submarine eruption  
83 (Carey et al., 2018; Chadwick et al., 2018, 2016; Clague et al., 2011; Perfit and Chadwick,  
84 1998; Resing et al., 2011; Rubin et al., 2012) and the third largest mafic eruption of the last two  
85 millennia after Eldgjá in 939 (Oppenheimer et al., 2018) and Laki in 1783-1784 (Thordarson  
86 and Self, 1993), both in Iceland.

87 The seismo-volcanic crisis began in May 2018 with a series of strong tectonic  
88 earthquakes, including 32 events with  $M_w \geq 5$ , located between 12 and 42 km depth,  $\sim 35$  km  
89 east of Mayotte (Cesca et al., 2020; Lemoine et al., 2020). On land, surface deformation

90 (subsidence and eastern motion) have been continuously observed since July 2018, and Very  
91 Long Period (VLP) seismic events related to fluid migration and possible magmatic activity  
92 have been occurring at least since mid-June 2018 (Cesca et al., 2020; Lemoine et al., 2020),  
93 suggesting that the eruptive activity has been ongoing for more than two years. On-going  
94 subsidence and seismicity have been linked to the eruption-related withdrawal of magma from  
95 its storage zone (Cesca et al., 2020; Feuillet et al., 2020; Lemoine et al., 2020).

96 Three oceanographic cruises (MAYOBS 1, Feuillet, (2019), MAYOBS 2, Jorry, (2019),  
97 MAYOBS 4, Fouquet and Feuillet (2019), Fig. 1c, d) between May and July 2019 provide an  
98 exceptional time-series of bathymetric, textural, petrological, and geochemical data for the  
99 2018-2019 eruptive period (Table 1). Since most mafic submarine eruptions are short-lived and  
100 have only been sampled after the end of the eruption, their study provides little information on  
101 their temporal evolution (Chadwick et al., 2018; Clague et al., 2018; Rubin et al., 2012). The  
102 geographically and temporally well-characterized sampling performed during the MAYOBS  
103 cruises thus brings an invaluable opportunity to better constrain the evolution of magma storage  
104 and transfer during a long-lived submarine eruption. In this paper, we present a detailed  
105 petrological, textural, and geochemical study of the submarine samples, to provide insights into  
106 the temporal and spatial evolution of a large volume of gas-rich magma rapidly intruding the  
107 lithosphere and reactivating multiple levels of magma storage. This is the first time that this  
108 methodology, developed for subaerial eruption at monitored volcanoes (Di Muro et al., 2014;  
109 Edmonds et al., 2013; Gansecki et al., 2019; Gurioli et al., 2018), and combining a large range  
110 of petrological and geochemical approaches on a temporal series of lava samples, is applied to  
111 a submarine eruption.

112

## 113 **2. GEOLOGICAL SETTING**

114

115       The Comoros Archipelago is located in the Mozambique Channel between the northern tip  
116 of Madagascar and the eastern coast of Mozambique (Fig. 1a). The four islands which compose  
117 the archipelago, Grande Comore, Moheli, Anjouan and Mayotte, are aligned on a NW-SE trend  
118 (Tzevahirtzian et al., 2020). This trend is superimposed on a zone of active seismicity  
119 connecting the northern extremity of Madagascar on the east, to the African coast to the west,  
120 and several authors suggest the presence of a boundary between the Lwandle microplate and  
121 the Somalia plate (Famin et al., 2020; Saria et al., 2014; Stamps et al., 2018). By combining a  
122 structural study with stress inversion of earthquake focal mechanisms, Famin et al. (2020)  
123 propose that this Lwandle and Somalian plate boundary is related to a complex E-W zone of  
124 immature right-lateral wrenching of the lithosphere.

125       Despite numerous studies, the origin of the volcanism in this geodynamic context remains  
126 a matter of debate (Bachèlery and Hémond, 2016; Class et al., 1998; Claude-Ivanaj et al., 1998;  
127 Coltorti et al., 1999; Deniel, 1998; Flower, 1973; Michon, 2016; Nougier et al., 1986; Pelleter  
128 et al., 2014; Strong, 1972; Thompson and Flower, 1971). Many hypotheses have been  
129 formulated including the interaction of a mantle plume with oceanic lithosphere (Class et al.,  
130 1998, 2005, 2009; Claude-Ivanaj et al., 1998; Emerick and Duncan, 1982; Hajash and  
131 Armstrong, 1972) and the reactivation of lithospheric structures possibly in relation with the  
132 East African Rift System (Lemoine et al., 2020; Michon, 2016; Nougier et al., 1986).

133       Trace elements and EM1 – HIMU isotopic signatures of volcanic rocks in the Comoros  
134 Archipelago would support the interaction of a mantle plume with amphibole/phlogopite-  
135 bearing oceanic metasomatized lithosphere (Bachèlery and Hémond, 2016; Class et al., 1998;  
136 Pelleter et al., 2014; Späth et al., 1996). However, the mantle plume hypothesis is considered  
137 incompatible with the migration of the African Plate towards the NNE and with the structural

138 features of the region (Famin et al., 2020). Finally, since the youngest volcanic activity occurs  
139 both in Grande Comore ( $0.13 \pm 0.02$  Ma to present; Hajash and Armstrong, 1972; Emerick and  
140 Duncan, 1982) with the active Karthala volcano (Bachelery et al., 2016) and in Mayotte (Cesca  
141 et al., 2020; Feuillet et al., 2020; Lemoine et al., 2020; Zinke et al., 2003), the age progression  
142 of volcanism is not consistent with formation of the archipelago by the migration of the Somali  
143 plate over a fixed hotspot. Several lines of evidence suggest that the volcanism of the Comoros  
144 archipelago is associated with lithospheric deformation rather than the result of a deep mantle  
145 plume (Famin et al., 2020; Lemoine et al., 2020; Michon, 2016).

146 Mayotte, the easternmost island of the archipelago, southwestward of Anjouan (Fig. 1a), is  
147 the oldest island with a maximum age of 20 Ma for the onset of subaqueous volcanic activity  
148 (Debeuf, 2004; Emerick and Duncan, 1982; Hajash and Armstrong, 1972; Michon, 2016;  
149 Nougier et al., 1986; Pelleter et al., 2014). It is composed of two main volcanic islands, Grande  
150 Terre and Petite Terre, the latter located 4 km east of Grande Terre. Mayotte subaerial activity  
151 is subdivided into multiple phases beginning in the southern part of Grande Terre (10.6 – 1.9  
152 Ma) and then migrating towards the north (5 – 0.75 Ma) and the northeast (0.75 – Present)  
153 separated by periods of quiescence (Debeuf, 2004; Nehlig et al., 2013; Pelleter et al., 2014).  
154 The current volcanic activity takes place 50 km off Mayotte, on a WNW-ESE submarine  
155 volcanic ridge on the east flank of the island, Fig. 1b, (Cesca et al., 2020; Feuillet et al., 2020;  
156 Lemoine et al., 2020).

157

### 158 **3. METHODS**

159

#### 160 *3.1. Sampling*

161 We first performed a high-resolution bathymetric survey of the eruptive site (Feuillet et  
162 al., 2019, 2021) to identify strategic dredging sites. Erupted lavas were dredged on five sites,  
163 each dredge running for about 100 – 600 m and returning a weight of approximately 300 – 900  
164 kg (Fig. 1c). During three oceanographic campaigns (MAYOBS 1, Feuillet, (2019), MAYOBS  
165 2, Jorry, (2019), MAYOBS 4, Fouquet and Feuillet (2019)), three dredges sampled the main  
166 volcanic cone and the radiating ridges built before May 2019 (phase 1: DR01, DR10, DR12,  
167 Table 1 and Fig. 1c, d), and two dredges on the S and SE flanks collected lava flows emitted  
168 during a second phase in June 2019 (DR08) and July 2019 (DR11). We selected fresh samples  
169 with representative morphologies and textures, including quenched pillow rims, pillow cores,  
170 sediments, samples containing xenoliths and phenocrysts. For this paper, we focused our study  
171 on glassy pillow rims that preserved the pre-quench textures, as well as xenoliths and  
172 phenocryst-rich fragments.

173

### 174 3.2. *Analytical techniques*

175 Bulk rock compositions were obtained on a set of 10 samples from 5 dredges (DR0101,  
176 DR0105, DR0801-ALF, DR080102, DR100511, DR11, DR1107(1), DR1107(2), DR110704-  
177 b and DR120202, Suppl. material Table 1). Major elements were analyzed on a HORIBA-  
178 Jobin-Yvon ULTIMA C ICP-AES at Laboratoire Magmas et Volcans (LMV, Clermont-  
179 Ferrand, France). Trace elements were analyzed on an Agilent 7900 ICP-MS at Institut de  
180 Physique du Globe de Paris (IPGP, Paris, France). In situ chemical analyses of minerals and  
181 glasses were performed using the CAMECA SXFive Tactis electron microprobe at LMV.  
182 Raman spectra were acquired on melt inclusions in olivine and magnetite, and on matrix glasses  
183 at the Ludwig Maximilian University (LMU – Laboratory of crystallography) using an XPlora

184 One spectrometer (Jobin Yvon) coupled with an Olympus microscope at 100x magnification.  
185 Details of the analytical procedures are presented in Supplementary Material “Methods”.

### 186 *3.3. Physical properties and textures*

187 Density measurements were performed on 27 lava samples using a Micromeritics  
188 Geopyc 1360 envelope density analyzer, following the procedure detailed by Thivet et al.  
189 (2020). The instrument measures the volume of particles with different sizes and shapes. These  
190 density measurements lead to reproducible data with a maximum standard deviation of  $\pm 30$   
191  $\text{kg}\cdot\text{m}^{-3}$  ( $1\sigma$ ) on five repeated measurements. The porosity of the samples was then calculated  
192 using vesicle-free rock density values (Houghton and Wilson, 1989) calculated from the partial  
193 molar volumes of oxide components (Bottinga and Weill, 1970). Petrographic observations and  
194 microtexture analysis were performed using optical microscope and scan. Vesicle and crystal  
195 size distribution (VSD and CSD), vesicle and crystal number density (NV and NC), and vesicle  
196 to melt ratio (VG/VL) were measured following the procedures in Shea et al. (2010) and  
197 assuming a spherical shape for both vesicles and crystals (mostly olivine).

### 198 *3.4. Fractional crystallization model*

199 Back-crystallization models were performed to reconstruct a potential mantle-derived  
200 parental melt. Equilibrium olivine and clinopyroxene were added in 1 wt % increments to the  
201 bulk composition of sample DR0101 until the melt was in equilibrium with a  $\text{Fo}_{90}$  mantle  
202 olivine. For each step, the composition of the equilibrium olivine was calculated from the  
203 magma composition of the previous step assuming a  $K_d$  of 0.30 ( $K_d = (\text{FeO}/\text{MgO})_{\text{olivine}} /$   
204  $(\text{FeO}/\text{MgO})_{\text{melt}}$ , Roeder and Emslie, (1970)) and a partition coefficient  $D_{\text{Ni}} = (\text{Ni}^{\text{olivine}} / \text{Ni}^{\text{melt}} =$   
205  $124 / \text{MgO} - 0.9$ , Hart and Davis, (1978)). The composition of the equilibrium clinopyroxene  
206 was calculated assuming a  $K_d$  of 0.28 (Putirka, 2008), oxides vs Mg# trends derived from a  
207 series of unpublished clinopyroxene analyses in basanite samples from Mayotte (Hassen Ali,

208 2020), and  $D_{Ni} = 2$ . The proportions of olivine and clinopyroxene were adjusted to fit the trend  
209 provided by a compilation of published bulk rock analyses from the Comoros Archipelago.

### 210 3.5. *Diffusion modelling*

211 Preliminary residence times were estimated using diffusion in zoned olivine crystals,  
212 modelled with the DIPRA software (Girona and Costa, 2013). Reversely zoned olivine crystals  
213 were oriented using an EBSD detector attached to a Zeiss Supra 55 VP field-emission scanning  
214 electron microscope housed at IStEP (Paris, France). Electron microprobe analyses were  
215 acquired along carefully selected profiles: we chose olivine crystals most likely to be cut close  
216 to their center (large homogeneous core), and the shortest possible profiles, perpendicular to  
217 euhedral faces and far from other faces, to avoid artificial lengthening of the profiles (e.g., Costa  
218 et al. 2008, Couperthwaite et al. 2021). Fo profiles (Fo = atomic  
219  $Mg/(Mg+Fe+Mn+Ca+Ni)*100$ ) were modelled using an average temperature of  $1095 \pm 20$  °C,  
220 an oxygen fugacity on the NNO buffer, and an arbitrary pressure of 200 MPa. Influence of  
221 pressure on diffusion times is within uncertainty.

222

## 223 4. RESULTS

224

### 225 4.1. Petrological and geochemical features

226 Bulk rock compositions of the lavas from the eruptive site fall within the compositional  
227 range of the moderately to slightly alkaline series of the Comoros archipelago, the “Karthala  
228 trend” (Bachèlery and Hémond, 2016; Class et al., 1998; Claude-Ivanaj et al., 1998; Coltorti et  
229 al., 1999; Deniel, 1998; Flower, 1973; Nougier et al., 1986; Pelleter et al., 2014; Strong, 1972;  
230 Thompson and Flower, 1971). They are silica-poor ( $46 < SiO_2$  wt.%  $< 48$ , Fig. 2a and Suppl.

231 material Table 1), and plot in the tephrite / basanite field of the TAS classification diagram.  
232 Since their normative olivine content is  $> 10\%$  they will be referred to as basanites in this study,  
233 although they are significantly evolved ( $4.4 < \text{MgO wt.}\% < 5.3$ ), and different from mantle-  
234 derived primitive basanites. Phase 2 lavas (DR08, DR11) are slightly more evolved than the  
235 earliest erupted ones with MgO content spanning a narrow range from 4.4 – 4.6 wt.%. All lavas  
236 analyzed are enriched in REE and other incompatible elements and display a steep chondrite-  
237 normalized REE pattern, close to the upper range found in the older subaerial Mayotte lavas  
238 (Fig. 2c).

239 Quenched samples are glassy, crystal-poor (4-6% crystals, Figs 3, 4, and Suppl. material  
240 Tables 2 and 3), and contain significant amounts of vesicle-trapped volatiles ("popping rocks").  
241 The average vesicularity of lavas is high, 35%, with a maximum of 43%, for phase 1 products  
242 (DR01-DR10-DR12) collected on the ridges radiating from the main edifice. Phase 2 lavas,  
243 collected on lava flows, are denser (average vesicularity of 31% for DR08, down to 18% for  
244 DR11). Except for DR11, these values are much higher than vesicularities of typical MORB  
245 popping rocks (Chavrit et al., 2014, 2012), but comparable with the few values measured for  
246 submarine alkali basalts. The average vesicularity for all investigated samples is 27 %. Using  
247 this average value, the 6.5 km<sup>3</sup> of the new volcano are equivalent to 4.8 km<sup>3</sup> of dense rock. Two  
248 binary images of lava fragments from the two textural endmembers (the most and the least  
249 vesicular lava) are shown in Fig. 3. DR0103a1 (Fig. 3b) from phase 1, is highly vesicular (43%)  
250 and characterized by a homogeneous population of rounded vesicles with a mean size of 0.4  
251 mm. The sample has a relatively high number of vesicles per unit of liquid ( $N_v$ , 17 mm<sup>-3</sup>). In  
252 contrast, DR110704b (Fig. 3a) is characterized by a lower vesicularity than DR01, with big,  
253 coalesced vesicles, up to 3 mm in diameter and a mean value of 0.8 mm and a drastic decrease  
254 in small vesicles, that translate in a low  $N_v$  (0.1 mm<sup>-3</sup>). A general decrease in number of vesicles  
255 is evident between the lava samples from phase 1 (DR01-DR10-DR12) and those from phase



256 2 (DR08-DR11), with DR11 samples being the lowest in terms of vesicularity and hence  
257 inferred pre-eruptive gas content (Fig. 3c).

258 Crystals in all samples include coeval Fe-rich olivine (50 – 790  $\mu\text{m}$ ,  $\text{Fo}_{69-73.5}$ ), Ti-  
259 magnetite (50 – 100  $\mu\text{m}$ ), and apatite (< 20  $\mu\text{m}$ , Fig. 4a, b). Rounded FeS droplets either  
260 included in olivine and magnetite crystals or directly in the glass indicate the presence of  
261 an immiscible sulphide liquid in some of the samples. Most crystals are euhedral, but skeletal  
262 crystals of olivine and titanomagnetite (Fig. 4b) are present in all samples, providing evidence  
263 for fast growth, likely linked to fast ascent rates. The small population of olivine phenocrysts,  
264 > 0.4 mm (for phase 1 samples) and > 1 mm (for phase 2 samples), represents a very low  
265 fraction of the total crystal population (0.3 – 1% of all olivine crystals). In samples from phase  
266 2 (June 2019 – July 2019, samples DR08 and DR11), some of the olivine phenocrysts are  
267 reversely zoned ( $\text{Fo}_{53}$  in the cores to  $\text{Fo}_{70}$  in the rims, Fig. 4c). Their rim composition is similar  
268 to that of olivine microlites (Fig. 4a, b).

269 The June 2019 lava flow (sample DR080205) contains small mantle xenoliths (Fig. 4d,  
270 e). The largest one (DR080205-x4) is ~5 mm in diameter, and composed of ~1 mm long crystals  
271 of  $\text{Fo}_{90}$  olivine and orthopyroxene with a Mg# (atomic  $(\text{Mg}/(\text{Mg}+\text{Fe}))\cdot 100$ ) of ~90 (Fig. 4d).  
272 Some of the orthopyroxene crystals contain clinopyroxene exsolutions. This xenolith also  
273 contains veins of  $\text{SiO}_2$ - and  $\text{K}_2\text{O}$ -rich silicate melts, typical of the melts produced by low-degree  
274 melting of phlogopite-bearing mantle (Condamine and Médard 2014). These melt veins are  
275 associated with small (< 100  $\mu\text{m}$ ) clinopyroxene crystals with Mg# between 92 and 94. A  
276 second and smaller xenolith (DR080205-x1), 2.5 mm long (Fig. 4e), is mostly composed of a  
277 single clinopyroxene crystal with orthopyroxene exsolutions, and small included crystals of  
278 olivine and orthopyroxene. Mineral compositions are similar to those in the first xenolith. A  
279 third investigated xenolith (DR080205-x3), only 2 mm in diameter, is similar to the first one,  
280 with mostly olivine and orthopyroxene crystals, and clinopyroxene exsolutions in the

281 orthopyroxene. All xenoliths reacted with the surrounding melts: pyroxene crystals react to  
282 form a fine-grained corona of clinopyroxene, olivine, and Ti-magnetite, while olivine crystals  
283 are overgrown by an Fo<sub>72</sub> olivine rim (Fig. 4d, e).

284 Sample DR080205 also contains a few clinopyroxene megacrysts (Fig. 4f). These  
285 megacrysts have a magmatic origin and show an inner, normally zoned core (Mg# 68– 61),  
286 surrounded by a more magnesian rim (Mg# 68 – 78). This magnesian rim shows evidence of  
287 dissolution and is in turn surrounded by an outer rim made of dendritic clinopyroxene crystals  
288 with interstitial glass (Fig. 4f).

289 Quantification of dissolved water has been performed by micro-Raman spectroscopy in  
290 melt inclusions hosted by olivine and titanomagnetite crystals. The pre-eruptive water content  
291 is constrained to a minimum of 2.3 wt. % for DR01 and 1.2 wt. % for DR08 (Fig. 5). Our  
292 preliminary data suggest that open embayments can retain high water contents comparable to  
293 those of the closed melt inclusions, suggesting the occurrence of disequilibrium water degassing  
294 during magma ascent. Disequilibrium water degassing typically results from fast magma ascent.  
295 It can be favored by the low crystal content, and in turn can delay melt crystallization and  
296 bubble nucleation (Ferguson et al., 2016; Lloyd et al., 2014).

297

## 298 **4.2. Thermobarometry**

299 Pre-eruptive temperatures for the main erupted magmas were calculated using the  
300 olivine-melt equilibrium and the equations of Beattie (1993) and Ford et al. (1983). Equilibrium  
301 olivine-glass pairs were selected based on a Fe/Mg Kd of  $0.30 \pm 0.05$ , assuming a Fe<sup>3+</sup>/Fe<sub>total</sub>  
302 ratio of 0.15, and the temperatures were averaged on 3 – 14 couples per sample. For  
303 thermometry calculations, the pressure was arbitrarily set at 200 MPa, however, the influence  
304 of pressure is limited to a few degrees per 100 MPa. Results from the model of Beattie (1993),

305 and from the  $T_{\text{sum}}$  equation of Ford et al. (1983) are within 2 – 8 °C of each other. Anhydrous  
306 calculated temperatures were corrected for the effect of H<sub>2</sub>O using average H<sub>2</sub>O concentration  
307 determined by micro-Raman spectrometry and the olivine liquidus depression model of Médard  
308 and Grove (2008). Uncorrected pre-eruptive temperatures are  $1151 \pm 20$  °C for phase 1 (DR01-  
309 DR10-DR12) and  $1136 \pm 20$  °C for phase 2 (DR08-DR11). Corrected temperatures are within  
310 error for all samples, at  $1095 \pm 20$  °C. Note that if melt inclusion provides a minimum pre-  
311 eruptive water content, this calculation provides a maximum pre-eruptive temperature.

312 Pre-eruptive temperature and oxygen fugacity for the magma batch parent to the Fo<sub>55</sub>  
313 olivine cores were calculated from an ilmenite-titanomagnetite intergrowth included in Fo<sub>55</sub>  
314 olivine, which constrains magmatic conditions of this evolved batch to  $1024 \pm 50$  °C and an  
315 oxygen fugacity (fO<sub>2</sub>) close to that of the nickel-nickel oxide buffer (Sauerzapf et al., 2008).  
316 Thermometry of melt inclusions in Fo<sub>52</sub> olivine gives similar anhydrous temperatures of about  
317  $1046 \pm 20$  °C (Beattie, 1993).

318 We analyzed a series of clinopyroxene-orthopyroxene pairs in the mantle xenoliths (Fig.  
319 4d, e) to obtain pressure and temperature constraints. In xenolith DR080205-x4, we analyzed  
320 clinopyroxene-orthopyroxene pairs associated with the high-SiO<sub>2</sub> high-K<sub>2</sub>O veins, as well as  
321 exsolutions of clinopyroxene in orthopyroxene. In the other two xenoliths, we only analyzed  
322 exsolutions, either of orthopyroxene in clinopyroxene (DR080205-x1), or of clinopyroxene in  
323 orthopyroxene (DR080205-x3). Temperatures were calculated using equation (36) of Putirka  
324 et al. (2008) with reported uncertainties of 45 °C. For pressure, both equations (38) and (39)  
325 were tested against experiments performed at 1.00 GPa by Condamine and Médard (2014) on  
326 pyroxene in equilibrium with high-SiO<sub>2</sub> high-K<sub>2</sub>O veins. Since equation (38) returned an  
327 average pressure of 1.02 GPa, whereas equation (39) returned an average pressure of 0.88,  
328 Equation (38) was preferred for the calculation. It reproduces the experimental data with an  
329 average error (SEE) of 0.19 GPa. Equilibration pressures for the xenoliths are 0.43 GPa at a

330 temperature of 926 °C for DR080205-x1 (Fig. 6a-c, Suppl. material Table 5), 0.41 GPa at a  
331 temperature of 890 °C for DR080205-x3 and 0.46 GPa at a temperature of 913 °C for  
332 DR080205-x4. Assuming an average density of 2890 kg m<sup>-3</sup> for an oceanic crust and 3300 kg  
333 m<sup>-3</sup> for the upper mantle, these xenoliths were equilibrated at an average depth below the sea  
334 level of 17 ± 6 km (0.45 ± 0.19 GPa).

335 We made an estimation of the magma storage depth by applying a clinopyroxene- only  
336 geobarometer (Equation 32b with water content of 2.3 wt.%, Putirka, 2008) to a zoned  
337 clinopyroxene megacryst in sample DR080502-x2 (Fig. 4f). The core of the crystal returns a  
338 depth range of 37 to 48 (P = 1.01 – 1.34 GPa). A second cluster with values ranging from 24 to  
339 34 (P = 0.62 – 0.92 GPa) is associated with the inner rim. A few low-pressure values (0.14 –  
340 0.38 GPa) were obtained on the outer dendritic rim and could indicate crystallization in the  
341 conduit during magma ascent (Fig. 6d). Uncertainties associated with these calculations are 10  
342 km (0.28 GPa, Putirka 2008). A second analyzed zoned clinopyroxene megacryst generates  
343 similar clusters. Phenocrysts in equilibrium with the bulk rock are expected to have Mg# of 75  
344 (olivine) and 78 (clinopyroxene), indicating that the most magnesian olivine cores and the  
345 clinopyroxene inner rims are in equilibrium with the magma. The more Fe-rich clinopyroxene  
346 cores should thus be interpreted as an antecrystic crystal cargo.

347

### 348 **4.3. Olivine diffusion and residence times**

349 Five different reversely zoned olivine crystals in DR0801-ALF, DR110704 and DR110401  
350 samples were investigated (Fig. 7a,b), assuming an initial step function with an olivine core  
351 between Fo<sub>53-60</sub> depending on the crystal, surrounded by an overgrowth rim Fo<sub>69-70</sub> (Fig. 7b).  
352 Two zoned olivine crystals at the edge of an harzburgite xenolith (DR080502x4) were also

353 modelled, using a step function with a Fo<sub>90</sub> olivine core and a Fo<sub>72</sub> olivine overgrowth (Fig.  
354 7c,d) but without EBSD orientation.

355 The five diffusion profiles in reversely zoned olivine crystals can be modelled with  
356 diffusion times of  $29 \pm 9$ ,  $24 \pm 8$ ,  $19 \pm 7$ ,  $38 \pm 12$  and  $40 \pm 11$  days (supplementary material  
357 Table 6, errors are given at the two sigma level). Since no EBSD data was acquired in the two  
358 normally zoned olivine crystals from xenolith DR080205x4, we can only provide a time bracket  
359 using maximum and minimum diffusion coefficient. Thus, these profiles can be modelled with  
360 diffusion times between 12 and 69 and between 8 and 47 days. Fits assuming instantaneous  
361 growth of the outer rims followed by pure diffusion are excellent with the reversely zoned  
362 crystals (supplementary material Table 6), and very good for the xenolith. The assumption of  
363 instantaneous crystal growth is supported by the orders of magnitude of difference between  
364 crystal growth rates and elemental diffusion rates (e.g., Petrone et al. 2016). These preliminary  
365 diffusion times can be interpreted as residence times for the olivine crystals and the xenolith,  
366 between injection of the incoming magma in the shallow magma pocket and its eruption at the  
367 surface.

368

## 369 **5. DISCUSSION**

370

### 371 **5.1. Source**

372

373 The magmas erupted during the ongoing Mayotte eruption are evolved basanite that likely  
374 derive from more primitive (unerupted) basanitic mantle melts. The low HREE concentrations  
375 and the strongly fractionated REE patterns ( $(\text{Tb/Yb})_{\text{N}} = 2.9 - 3.2$ , Fig. 2c) indicate the presence  
376 of residual garnet in the mantle source. Moreover, Sm/Yb and La/Sm ratios for the erupted

377 lavas indicate a spinel/garnet lherzolitic source (Fig. 2d). This is consistent with previous  
378 studies on subaerial Comoros lavas which suggest that primary magmas are produced by small  
379 degrees of partial melting at the depth of the spinel to garnet lherzolite transition, 80 – 100 km  
380 (Bachèlery and Hémond, 2016; Class et al., 1998). Furthermore, olivine melilitites in Mayotte  
381 volcanic products and evidence of metasomatizing carbonatitic fluids on Grande Comore  
382 suggest a CO<sub>2</sub>-rich mantle source (Coltorti et al., 1999; Pelleter et al., 2014). The P<sub>2</sub>O<sub>5</sub>  
383 enrichment of the new volcano samples, together with the high Sr and Ba contents, and high  
384 Nb/Yb ratio, are consistent with an apatite contribution in the genesis of these lavas. Presence  
385 of a mm-sized apatite xenocryst in one of our lava samples suggests a possible assimilation of  
386 apatite-bearing veins during the ascent of primary melts formed at a greater depth, as indicated  
387 by Pelleter et al., (2014). Homogeneous P<sub>2</sub>O<sub>5</sub> enrichment compared to other Comoros lavas is  
388 observed in all of our samples (1.6 – 2.0 wt.%, Suppl. material Table 1), which precludes a late  
389 assimilation and argues for a mantle source origin of the inferred apatite-bearing veins.

390

## 391 **5.2. Deep magma reservoir in the lithospheric mantle**

392 The evolved nature (low Mg#, 43 – 47) of the erupted magmas shows that they are not  
393 primary products of mantle melting since the expected Mg# of primary mantle melts in  
394 equilibrium with Fo<sub>90</sub> olivine is ~73, assuming an olivine/melt Kd of 0.30 (Roeder and Emslie,  
395 1970). Extensive cooling and crystallization must thus have occurred in a lithospheric magma  
396 reservoir (Fig. 8). A back-crystallization model consistent with the general trend of Comoros  
397 lavas (Bachèlery and Hémond, 2016; Class et al., 1998; Claude-Ivanaj et al., 1998; Coltorti et  
398 al., 1999; Deniel, 1998; Flower, 1973; Nougier et al., 1986; Pelleter et al., 2014; Strong, 1972;  
399 Thompson and Flower, 1971) requires approximately 50% crystallization of an olivine-  
400 clinopyroxene assemblage (80% clinopyroxene Mg#<sub>91-76</sub> and 20% olivine Fo<sub>90-75</sub>) to reproduce

401 the erupted magma compositions (Fig. 2b). This implies that the reservoir, where mantle-  
402 derived magma is ponding and differentiating, has a volume of at least  $\sim 10 \text{ km}^3$  ( $\sim 5 \text{ km}^3$  of  
403 erupted magma and the same amount of crystals) and is zoned, with  $\sim 5 \text{ km}^3$  of residual dense  
404 cumulates. This is a minimum reservoir size, since the estimation relies on the unlikely  
405 hypothesis that melt and cumulates were perfectly segregated, and does not take into account  
406 any interstitial melt within the cumulates and the contribution of deep  $\text{CO}_2$  exsolution. The  
407 occurrence of a large reservoir is also supported by ratios of intrusive to extrusive volumes  
408 commonly estimated at  $\sim 5:1$  for oceanic mid-ocean ridges (Crisp, 1984; White et al., 2006).  
409 Since the erupted magma was a true homogeneous liquid, and the few crystals of the main cone-  
410 building phase 1 are unzoned, this suggests the system was not disturbed by new primary  
411 magma replenishment and was able to evolve to yield a single well-stratified reservoir. In  
412 sample DR080205-x2, clinopyroxene megacryst cores were equilibrated at pressures of 1.01 –  
413 1.34 GPa (from Putirka, 2008, equation 32b, i.e. 37 – 48 km, Figs 6d and 8). This provides the  
414 depth for the main reservoir feeding the current eruption, which is thus located in the  
415 lithospheric mantle, in agreement with seismological and geodetic models (Cesca et al., 2020;  
416 Lemoine et al., 2020). The slowly waning effusion rate is also characteristic of an eruption fed  
417 by a deep reservoir (Wadge, 1981).

418 Magma ascending from lithospheric mantle storage entrained mantle xenoliths from a  
419 shallower depth, near the Moho, at an average depth of  $17 \pm 6 \text{ km}$ . The time between  
420 entrainment of the mantle xenoliths and eruption is estimated less than 70 days. Given that the  
421 xenoliths were picked up en route to the surface, this is a preliminary estimation of the transfer  
422 time between the deep magma reservoir and the eruption site. It is consistent with the 6 weeks  
423 of precursory unrest estimated from seismological data (Cesca et al., 2020; Lemoine et al.,  
424 2020).

425

### 5.3. Differentiated shallower magma batch

427 Phase 1 products are crystal-poor lavas with high density of vesicles (Fig. 3b), skeletal  
428 crystals (Fig. 4a, b) and high dissolved water content (Fig. 5). Thus, we suggest that during the  
429 first year, eruption is fed by direct ascent of magma from the deep reservoir to the surface. The  
430 shape and the size of microlites indicate that most micro-crystallization occurred in the shallow  
431 part of the ascending dyke. The degree of magmatic evolution increases from phase 1 to phase  
432 2 lavas (Fig. 1d). This increase is mirrored by a decrease in vesicularity, vesicle number density  
433 (Fig. 3) and dissolved water content (Fig. 5), indicating that late erupted lavas were increasingly  
434 outgassed. Reverse zoning in olivine phenocrysts from phase 2 lavas (Fig. 4c) records the  
435 interaction between the hot basanitic magma, ascending from the  $\geq 37$  km deep storage zone,  
436 and a second cooler magma batch (Fig. 8). Since transfer times estimated from diffusion in  
437 those crystals ( $\sim 1$  month) are similar to transfer times estimated from the mantle xenoliths, the  
438 zoned olivine crystals probably came from a similar or shallower depth than the xenoliths.  
439 Pyroxenes in the mantle xenoliths record a depth of  $17 \pm 6$  km, interpreted to represent the  
440 maximum depth of this shallower reservoir (Fig. 6). The inner rim in clinopyroxene megacryst  
441 (DR080205-x4, Fig. 4f), equilibrated at pressures of  $0.8 \pm 0.28$  GPa ( $28 \pm 10$  km), may indicate  
442 the location of a third magma storage zone.

443 Because no seismicity at this shallow depth was detected (ReVoSiMa, 2021), the  
444 differentiated magma batch is unlikely to occupy a large dynamic reservoir but rather perhaps  
445 magma ponding at the base of the Moho. Analysis of diffusion profiles in reversely zoned  
446 olivine from phase 2 lava flows constrain the time between the start of Fo<sub>70</sub> olivine  
447 crystallization and eruption. We obtain minimum estimations of  $\sim 1$  month for the time between  
448 mixing with the shallower magma batch and eruption of the hybrid magma (Fig. 7, Suppl.  
449 material Table 6). Magma mixing and transfer of hybrid magma thus occurred during the



450 eruption and were not related to long-term precursor activity detected by the permanent land-  
451 based monitoring networks.

452

#### 453 **5.4. Eruption trigger**

454 The erupted products are evolved alkaline mafic magmas and have a minimum  
455 dissolved water content of ca. 2 wt. % (Fig. 5). Available thermodynamic models permit us to  
456 crudely estimate the pre-eruptive dissolved CO<sub>2</sub> content as being in the range 0.6 – 1.2 wt %  
457 (Allison et al., 2019; Papale et al., 2006). This is compatible with the possible presence of an  
458 exsolved CO<sub>2</sub>-rich fluid phase in the plumbing system. Under these conditions, the magma  
459 chamber will be pressurized, but stable. Because of the deep location and the associated  
460 pressure, volume changes due to crystallization or volatile exsolution should not be sufficient  
461 to act as an eruption trigger. Moreover, we found no evidence of primitive magma in the erupted  
462 products. Therefore, we suggest that fault movement or earthquakes rather than a deep reservoir  
463 recharge event was responsible for the sudden initial decompression and fast ascent of a large  
464 volume of volatile-rich melt stored in the mantle.

465 The eruption site belongs to a WNW-ESE volcano-tectonic ridge, parallel to regional  
466 trends, suggesting relation to a pre-existing tectonic structure. Deep seismicity recorded during  
467 the seismo-volcanic crisis (Cesca et al., 2020; Lemoine et al., 2020; ReVoSiMa, 2021) implies  
468 that these structures are deeply rooted in the lithosphere (up to 50 km depth). The sequence of  
469 strong tectonic earthquakes recorded at the beginning of the eruption (volcano-tectonic events  
470 located at 34 – 41 km depth, 35 km east of Mayotte (Cesca et al., 2020; Lemoine et al., 2020)  
471 might thus be related to the movement along the lithospheric faults.

472

## 473 5.5. Syn-eruptive magma path change

474 Since the melt was volatile-saturated ( $\text{CO}_2+\text{H}_2\text{O}$ ) in the deep reservoir, magma ascent  
475 towards the surface would have resulted in continuous exsolution of  $\text{CO}_2$  first and then  
476  $\text{CO}_2+\text{H}_2\text{O}$  up to the eruption site. Full exsolution of pre-eruptive dissolved volatiles at the vent  
477 would produce a fluid with a molar volume of ca.  $320 \text{ cm}^3/\text{mol}$  and vesicularity in the range 54  
478 – 71 vol%, values much higher than those measured in our samples (Suppl. material Tables 2  
479 and 3). Vesicularity would be even higher if there were additional exsolved  $\text{CO}_2$  in the reservoir.  
480 Incomplete disequilibrium degassing because of the fast ascent rate and rapid quenching on the  
481 seafloor can explain the difference between the expected and measured vesicularities. We also  
482 suggest that rapid decompression-induced crystallization (Hammer et al., 1999) in the shallow  
483 conduit may be responsible for the skeletal shape of olivine and Ti-magnetite crystals (Faure et  
484 al., 2003). The absence of reversely zoned olivine crystals in phase 1 products suggests that  
485 basaltic melts ascended from the deep reservoir directly to the surface during the first year of  
486 eruption (Fig. 8).

487 In contrast, the presence of reversely zoned olivine with  $\text{Fo}_{53}$  cores in phase 2 lava flows  
488 (Fig. 4c) indicates that, after May 2019 magma ascending from the deep reservoir intersected a  
489 more evolved magma batch, at a depth near the Moho on its way to the surface (Fig. 8). Using  
490 a simple mass balance model, we estimate that only 6% of the evolved magma (represented by  
491 melt inclusions in  $\text{Fo}_{53}$  olivine in sample DR11) was assimilated in the erupted lavas, indicating  
492 that the intersected volume of this shallower reservoir is much smaller than the deeper one. Less  
493 abundant (low  $N_v$ ) and larger vesicles (Fig. 3) are consistent with a slower ascent and lower  
494 volatile content during phase 2. The residual magmatic liquid in the shallower magma batch  
495 could have been produced by fractional crystallization from an older magma intrusion, as  
496 observed during Kilauea's 2018 eruption (Gansecki et al., 2019). Due to the time required for  
497 magmatic differentiation (decades, Gansecki et al., 2019), this observation implies magma

498 intrusion and possible recent volcanic activity in the offshore part of the volcanic ridge prior to  
499 the current eruption. The emission of the more evolved magma in phase 2 could have resulted  
500 either from a change in the dyke pathway (as suggested by the presence of mantle xenoliths)  
501 and/or a decrease in magma discharge rate allowing the input from the second shallower magma  
502 source.

503 Zoned olivine phenocrysts took  $\sim 1$  month to be transferred from the  $\sim 17$  km shallow  
504 reservoir to the seafloor. Thus, we obtain a minimum ascent rate of  $0.005 \text{ m.s}^{-1}$  from the shallow  
505 reservoir to the surface for the slower pathway (Fig. 8).

506

## 507 **6. CONCLUSIONS**

508 The large and long-lasting effusive eruption offshore from Mayotte is fed by a deep ( $>$   
509  $37 \text{ km}$ ) and large ( $\geq 10 \text{ km}^3$ ) pre-existing mantle reservoir of evolved, alkaline magma that  
510 experienced extensive crystallization. This has important volcanic hazard implications, because  
511 it demonstrates that this large, volatile-rich deep reservoir could quickly be tapped in a  
512 tectonically active region to feed a voluminous and long-lasting effusive eruption. During the  
513 eruption, magma ascent slowed and switched to a pathway that sampled a small more  
514 chemically evolved shallower magma batch at the base of the crust. Our petrological study  
515 provides important constraints on the entire deep magmatic system from the source to the  
516 surface. These results bring valuable and critical information complementary to geophysical  
517 datasets, showing that we can use the petrology of erupted products for long-term monitoring  
518 of extreme events even when they occur in poorly accessible environments. These data helped  
519 to determine the geometry and the dynamics of magmatic plumbing systems, and provided  
520 critical constraints for the interpretation of geophysical datasets in terms of processes and  
521 patterns.

522

## 523 **Acknowledgements**

524 MAYOBS 1 campaign was funded by the CNRS-INSU TELLUS MAYOTTE program  
525 (SISMAYOTTE project). MAYOBS 1, 2 and 4 campaigns were conducted by several French  
526 research institutions and laboratories (IPGP/CNRS/BRGM/IFREMER/IPGS). We want to  
527 thank the crew of R/V Marion Dufresne (TAAF/IFREMER/LDA). Analyses were funded by  
528 the Service National d'Observation en Volcanologie (SNOV, INSU) and the Réseau de  
529 Surveillance Volcanologique et Sismologique de Mayotte (REVOSIMA), a partnership  
530 between the Institut de Physique du Globe de Paris (IPGP), the Bureau de Recherches  
531 Géologiques et Minières (BRGM), and the Observatoire Volcanologique du Piton de la  
532 Fournaise (OVPF-IPGP), the Centre National de la Recherche Scientifique (CNRS), and the  
533 Institut Français de Recherche pour l'Exploitation de la Mer (IFREMER). The authors would  
534 like to thank Andrew Harris for reviewing and English improvement before submission,  
535 IFREMER for their welcome during the sampling and E. Humler for his support and national  
536 funding coordination (CNRS, REVOSIMA). Raman data were acquired by ADM as a side  
537 project during his fellowship at the Center for Advanced Studies of the Ludwig-Maximilians-  
538 Universität München (CAS LMU) in collaboration with the CAS Research Group on "Magma  
539 to Tephra: Ash in the Earth System" (Resp. Prof. Donald Dingwell). We thank Ivonne Cocca  
540 (Université de Paris) for assistance in sample preparation. Finally, we are also grateful for the  
541 helpful reviews provided by William Chadwick, an anonymous reviewer, and editorial handling  
542 by Chiara Petrone. This is a Labex ClerVolc contribution number 466.

## 543 **References**

544 Allison, C.M., Roggensack, K., Clarke, A.B., 2019. H<sub>2</sub>O–CO<sub>2</sub> solubility in alkali-rich mafic  
545 magmas: new experiments at mid-crustal pressures. *Contrib. Mineral. Petrol.* 174, 58.  
546 <https://doi.org/10.1007/s00410-019-1592-4>

- 547 Bachèlery, P., Hémond, C., 2016. Geochemical and Petrological Aspects of Karthala Volcano,  
548 in: *Active Volcanoes of the Southwest Indian Ocean*. Springer, pp. 367–384.
- 549 Bachèlery, P., Morin, J., Villeneuve, N., Soulé, H., Nassor, H., Ali, A.R., 2016. Structure and  
550 eruptive history of Karthala volcano, in: *Active Volcanoes of the Southwest Indian Ocean*.  
551 Springer, pp. 345–366.
- 552 Beattie, P., 1993. Olivine-melt and orthopyroxene-melt equilibria. *Contrib. Mineral. Petrol.*  
553 115, 103–111. <https://doi.org/10.1007/BF00712982>
- 554 Bottinga, Y., Weill, D.F., 1970. Densities of liquid silicate systems calculated from partial  
555 molar volumes of oxide components. *Am. J. Sci.* 269, 169–182.
- 556 Carey, R., Soule, S.A., Manga, M., White, J.D.L., McPhie, J., Wysoczanski, R., Jutzeler, M.,  
557 Tani, K., Yoerger, D., Fornari, D., 2018. The largest deep-ocean silicic volcanic eruption  
558 of the past century. *Sci. Adv.* 4, e1701121. <https://doi.org/10.1126/sciadv.1701121>
- 559 Cesca, S., Letort, J., Razafindrakoto, H.N.T., Heimann, S., Rivalta, E., Isken, M.P., Nikkhoo,  
560 M., Passarelli, L., Petersen, G.M., Cotton, F., Dahm, T., 2020. Drainage of a deep magma  
561 reservoir near Mayotte inferred from seismicity and deformation. *Nat. Geosci.* 13, 87–93.  
562 <https://doi.org/10.1038/s41561-019-0505-5>
- 563 Chadwick, W.W., Merle, S.G., Baker, E.T., Walker, S.L., Resing, J.A., Butterfield, D.A.,  
564 Anderson, M.O., Baumberger, T., Bobbitt, A.M., 2018. A recent volcanic eruption  
565 discovered on the central Mariana back-arc spreading center. *Front. Earth Sci.* 6, 172.  
566 <https://doi.org/10.3389/feart.2018.00172>
- 567 Chadwick, W.W., Paduan, J.B., Clague, D.A., Dreyer, B.M., Merle, S.G., Bobbitt, A.M.,  
568 Caress, D.W., Philip, B.T., Kelley, D.S., Nooner, S.L., 2016. Voluminous eruption from  
569 a zoned magma body after an increase in supply rate at Axial Seamount. *Geophys. Res.*  
570 *Lett.* 43, 12063–12070. <https://doi.org/10.1002/2016GL071327>.
- 571 Chavrit, D., Humler, E., Grasset, O., 2014. Mapping modern CO<sub>2</sub> fluxes and mantle carbon  
572 content all along the mid-ocean ridge system. *Earth Planet. Sci. Lett.* 387, 229–239.  
573 <https://doi.org/10.1016/j.epsl.2013.11.036>
- 574 Chavrit, D., Humler, E., Morizet, Y., Laporte, D., 2012. Influence of magma ascent rate on  
575 carbon dioxide degassing at oceanic ridges: Message in a bubble. *Earth Planet. Sci. Lett.*  
576 357, 376–385. <https://doi.org/10.1016/j.epsl.2012.09.042>
- 577 Clague, D.A., Paduan, J.B., Caress, D.W., Thomas, H., Chadwick Jr, W.W., Merle, S.G., 2011.  
578 Volcanic morphology of West Mata Volcano, NE Lau Basin, based on high-resolution  
579 bathymetry and depth changes. *Geochemistry, Geophys. Geosystems* 12.  
580 <https://doi.org/10.1029/2011GC003791>
- 581 Clague, D.A., Paduan, J.B., Dreyer, B.M., Chadwick Jr, W.W., Rubin, K.R., Perfit, M.R.,  
582 Fundis, A.T., 2018. Chemical variations in the 1998, 2011, and 2015 lava flows from Axial  
583 Seamount, Juan de Fuca Ridge: Cooling during ascent, lateral transport, and flow.  
584 *Geochemistry, Geophys. Geosystems* 19, 2915–2933.  
585 <https://doi.org/10.1029/2018GC007708>
- 586 Class, C., Goldstein, S.L., Altherr, R., Bachèlery, P., 1998. The process of plume–lithosphere  
587 interactions in the ocean basins—the case of Grande Comore. *J. Petrol.* 39, 881–903.  
588 <https://doi.org/10.1093/etroj/39.5.881>

- 589 Class, C., Goldstein, S.L., Shirey, S.B., 2009. Osmium isotopes in Grande Comore lavas: a new  
590 extreme among a spectrum of EM-type mantle endmembers. *Earth Planet. Sci. Lett.* 284,  
591 219–227. <https://doi.org/10.1016/j.epsl.2009.04.031>
- 592 Class, C., Goldstein, S.L., Stute, M., Kurz, M.D., Schlosser, P., 2005. Grand Comore Island: A  
593 well-constrained “low  $^3\text{He}/^4\text{He}$ ” mantle plume. *Earth Planet. Sci. Lett.* 233, 391–409.  
594 <https://doi.org/10.1016/j.epsl.2005.02.029>
- 595 Claude-Ivanaj, C., Bourdon, B., Allègre, C.J., 1998. Ra–Th–Sr isotope systematics in Grande  
596 Comore Island: a case study of plume–lithosphere interaction. *Earth Planet. Sci. Lett.* 164,  
597 99–117. [https://doi.org/10.1016/S0012-821X\(98\)00195-2](https://doi.org/10.1016/S0012-821X(98)00195-2)
- 598 Coltorti, M., Bonadiman, C., Hinton, R.W., Siena, F., Upton, B.G.J., 1999. Carbonatite  
599 metasomatism of the oceanic upper mantle: evidence from clinopyroxenes and glasses in  
600 ultramafic xenoliths of Grande Comore, Indian Ocean. *J. Petrol.* 40, 133–165.  
601 <https://doi.org/10.1016/j.epsl.2014.04.027>
- 602 Condamine, P., Médard, E., 2014. Experimental melting of phlogopite-bearing mantle at 1 GPa:  
603 Implications for potassic magmatism. *Earth Planet. Sci. Lett.* 397, 80–92.  
604 <https://doi.org/10.1016/j.epsl.2014.04.027>
- 605 Crisp, J.A., 1984. Rates of magma emplacement and volcanic output. *J. Volcanol. Geotherm.*  
606 *Res.* 20, 177–211. [https://doi.org/10.1016/0377-0273\(84\)90039-8](https://doi.org/10.1016/0377-0273(84)90039-8)
- 607 Costa, F., Dohmen, R., Chakraborty, S., 2008. Time scales of magmatic processes from  
608 modeling the zoning patterns of crystals. *Rev. Mineral. Geochemistry* 69, 545–594.  
609 <https://doi.org/10.2138/rmg.2008.69.14>
- 610 Couperthwaite, F.K., Morgan, D.J., Pankhurst, M.J., Lee, P.D., Day, J.M.D., 2021. Reducing  
611 epistemic and model uncertainty in ionic inter-diffusion chronology: A 3D observation  
612 and dynamic modeling approach using olivine from Piton de la Fournaise, La Réunion.  
613 *Am. Mineral. J. Earth Planet. Mater.* 106, 481–494. <https://doi.org/10.2138/am-2021-7296CCBY>
- 614
- 615 Debeuf, D., 2004. Étude de l'évolution volcano-structurale et magmatique de Mayotte (archipel  
616 des Comores, océan Indien). PhD thesis, Université de la Réunion, France.
- 617 Deniel, C., 1998. Geochemical and isotopic (Sr, Nd, Pb) evidence for plume–lithosphere  
618 interactions in the genesis of Grande Comore magmas (Indian Ocean). *Chem. Geol.* 144,  
619 281–303. [https://doi.org/10.1016/S0009-2541\(97\)00139-3](https://doi.org/10.1016/S0009-2541(97)00139-3)
- 620 Di Muro, A., Métrich, N., Vergani, D., Rosi, M., Armienti, P., Fougereux, T., Deloule, E.,  
621 Arienzo, I., Civetta, L., 2014. The shallow plumbing system of Piton de la Fournaise  
622 Volcano (La Reunion Island, Indian Ocean) revealed by the major 2007 caldera-forming  
623 eruption. *J. Petrol.* 55, 1287–1315. <https://doi.org/10.1093/petrology/egu025>
- 624 Di Muro, A., Villemant, B., Montagnac, G., Scaillet, B., Reynard, B., 2006. Quantification of  
625 water content and speciation in natural silicic glasses (phonolite, dacite, rhyolite) by  
626 confocal microRaman spectrometry. *Geochim. Cosmochim. Acta* 70, 2868–2884.  
627 <https://doi.org/10.1016/j.gca.2006.02.016>
- 628 Dofal, A., Fontaine, F.R., Michon, L., Barruol, G., Tkalcic, H., 2018. Crustal structure variation  
629 across the southwestern Indian Ocean from receiver functions determined at Ocean-  
630 Bottom Seismometers, in: AGU Fall Meeting 2018. AGU.

- 631 Edmonds, M., Sides, I.R., Swanson, D.A., Werner, C., Martin, R.S., Mather, T.A., Herd, R.A.,  
632 Jones, R.L., Mead, M.I., Sawyer, G., 2013. Magma storage, transport and degassing during  
633 the 2008–10 summit eruption at Kīlauea Volcano, Hawai‘i. *Geochim. Cosmochim. Acta*  
634 123, 284–301. <https://doi.org/10.1016/j.gca.2013.05.038>
- 635 Emerick, C.M., Duncan, R.A., 1982. Age progressive volcanism in the Comores Archipelago,  
636 western Indian Ocean and implications for Somali plate tectonics. *Earth Planet. Sci. Lett.*  
637 60, 415–428. [https://doi.org/10.1016/0012-821X\(82\)90077-2](https://doi.org/10.1016/0012-821X(82)90077-2)
- 638 Famin, V., Michon, L., Bourhane, A., 2020. The Comoros archipelago: a right-lateral transform  
639 boundary between the Somalia and Lwandle plates. *Tectonophysics* 789, 228539.  
640 <https://doi.org/10.1016/j.tecto.2020.228539>
- 641 Faure, F., Trolliard, G., Nicollet, C., Montel, J.-M., 2003. A developmental model of olivine  
642 morphology as a function of the cooling rate and the degree of undercooling. *Contrib.*  
643 *Mineral. Petrol.* 145, 251–263. <https://doi.org/10.1007/s00410-003-0449-y>
- 644 Ferguson, D.J., Gonnermann, H.M., Ruprecht, P., Plank, T., Hauri, E.H., Houghton, B.F.,  
645 Swanson, D.A., 2016. Magma decompression rates during explosive eruptions of Kīlauea  
646 volcano, Hawaii, recorded by melt embayments. *Bull. Volcanol.* 78, 71.  
647 <https://doi.org/10.1007/s00445-016-1064-x>
- 648 Feuillet, N., 2019. MAYOBS1 cruise, RV Marion Dufresne.  
649 <https://doi.org/10.17600/18001217>
- 650 Feuillet, N., Jorry, S., Rinnert, E., Thinon, I., Fouquet, Y., 2019. MAYOBS cruises, RV Marion  
651 Dufresne. <https://doi.org/10.18142/291>
- 652 Feuillet, N., Jorry, S.J., Crawford, W., Deplus, C., Thinon, I., Jacques, E., Saurel, J.M.,  
653 Lemoine, A., Paquet, F., Satriano, C., Aiken, C., Foix, O., Kowalski, P., Laurent, A.,  
654 Rinnert, E., Cathalot, C., Donval, J.P., Guyader, V., Gaillot, A., Scalabrin, C., Moreira,  
655 M., Peltier, A., Beauducel, F., Grandin, R., Ballu, V., Daniel, R., Pelleau, P., Gomez, J.,  
656 Besançon, S., Geli, L., Bernard, P., Bachelery, P., Fouquet, Y., Bertil, D., Lemarchand,  
657 A., van der Woerd, J., 2020. Birth of a large volcanic edifice through lithosphere-scale  
658 diking offshore Mayotte (Indian Ocean). *EarthArXiv*. <https://doi.org/10.31223/X5B89P>
- 659 Flower, M.F.J., 1973. Evolution of basaltic and differentiated lavas from Anjouan, Comores  
660 Archipelago. *Contrib. to Mineral. Petrol.* 38, 237–260.
- 661 Ford, C.E., Russell, D.G., Craven, J.A., Fisk, M.R., 1983. Olivine-liquid equilibria:  
662 temperature, pressure and composition dependence of the crystal/liquid cation partition  
663 coefficients for Mg, Fe<sup>2+</sup>, Ca and Mn. *J. Petrol.* 24, 256–266.  
664 <https://doi.org/10.1093/petrology/24.3.256>
- 665 Fouquet, Y., Feuillet, N., 2019. MAYOBS4 cruise, RV Marion Dufresne.  
666 <https://doi.org/10.17600/18001238>
- 667 Gansecki, C., Lee, R.L., Shea, T., Lundblad, S.P., Hon, K., Parcheta, C., 2019. The tangled tale  
668 of Kīlauea’s 2018 eruption as told by geochemical monitoring. *Science* (80-. ). 366.  
669 <https://doi.org/10.1126/science.aaz0147>
- 670 Girona, T., Costa, F., 2013. DIPRA: A user-friendly program to model multi-element diffusion  
671 in olivine with applications to timescales of magmatic processes. *Geochemistry, Geophys.*  
672 *Geosystems* 14, 422–431. <https://doi.org/10.1029/2012GC004427>

- 673 Gurioli, L., Di Muro, A., Vlastélic, I., Moune, S., Thivet, S., Valer, M., Villeneuve, N.,  
674 Boudoire, G., Peltier, A., Bachèlery, P., 2018. Integrating field, textural, and geochemical  
675 monitoring to track eruption triggers and dynamics: a case study from Piton de la  
676 Fournaise. *Solid Earth* 9, 431–455. <https://doi.org/10.5194/se-9-431-2018>
- 677 Hajash, A., Armstrong, R.L., 1972. Paleomagnetic and radiometric evidence for the age of the  
678 Comores Islands, west central Indian Ocean. *Earth Planet. Sci. Lett.* 16, 231–236.  
679 [https://doi.org/10.1016/0012-821X\(72\)90195-1](https://doi.org/10.1016/0012-821X(72)90195-1)
- 680 Hammer, J.E., Cashman, K. V, Hoblitt, R.P., Newman, S., 1999. Degassing and microlite  
681 crystallization during pre-climactic events of the 1991 eruption of Mt. Pinatubo,  
682 Philippines. *Bull. Volcanol.* 60, 355–380. <https://doi.org/10.1007/s004450050238>
- 683 Hart, S.R., Davis, K.E., 1978. Nickel partitioning between olivine and silicate melt. *Earth*  
684 *Planet. Sci. Lett.* 40, 203–219.
- 685 Hassen Ali, T., 2020. Etude pétrochimique du volcanisme récent de Mayotte. Master thesis,  
686 Université Clermont Auvergne, Clermont-Ferrand, France.
- 687 Houghton, B.F., Wilson, C.J.N., 1989. A vesicularity index for pyroclastic deposits. *Bull.*  
688 *Volcanol.* 51, 451–462. <https://doi.org/10.1007/BF01078811>
- 689 Jorry, S.J., 2019. MAYOBS2 cruise, RV Marion Dufresne. <https://doi.org/10.17600/18001222>
- 690 Lemoine, A., Briole, P., Bertil, D., Roullé, A., Foumel, M., THINON, I., Raucoules, D.,  
691 Michele, M. de, Valty, P., 2020. The 2018-2019 seismo-volcanic crisis east of Mayotte,  
692 Comoros islands: seismicity and ground deformation markers of an exceptional submarine  
693 eruption. *Geophys. J. International* 223(1): 22-44. <https://doi.org/10.31223/osf.io/d46xj>
- 694 Lloyd, A.S., Ruprecht, P., Hauri, E.H., Rose, W., Gonnermann, H.M., Plank, T., 2014.  
695 NanoSIMS results from olivine-hosted melt embayments: magma ascent rate during  
696 explosive basaltic eruptions. *J. Volcanol. Geotherm. Res.* 283, 1–18.  
697 <https://doi.org/10.1016/j.jvolgeores.2014.06.002>
- 698 Médard, E., Grove, T.L., 2008. The effect of H<sub>2</sub>O on the olivine liquidus of basaltic melts:  
699 experiments and thermodynamic models. *Contrib. Mineral. Petrol.* 155, 417–432.  
700 <https://doi.org/10.1007/s00410-007-0250-4>
- 701 Michon, L., 2016. The volcanism of the Comoros archipelago integrated at a regional scale, in:  
702 *Active Volcanoes of the Southwest Indian Ocean*. Springer, pp. 333–344.  
703 [https://doi.org/10.1007/978-3-642-31395-0\\_21](https://doi.org/10.1007/978-3-642-31395-0_21)
- 704 Nehlig, P., Lacquement, F., Bernard, J., Caroff, M., Deparis, J., Jaouen, T., Pelleter, A.A.,  
705 Perrin, J., Prognon, C., Vittecoq, B., 2013. Notice de la carte géologique de Mayotte.  
706 BRGM/RP-61803-FR, 135 p., 45 ill., 1 ann.
- 707 Nougier, J., Cantagrel, J.M., Karche, J.P., 1986. The Comores archipelago in the western Indian  
708 Ocean: volcanology, geochronology and geodynamic setting. *J. African Earth Sci.* 5, 135–  
709 144. [https://doi.org/10.1016/0899-5362\(86\)90003-5](https://doi.org/10.1016/0899-5362(86)90003-5)
- 710 Oppenheimer, C., Orchard, A., Stoffel, M., Newfield, T.P., Guillet, S., Corona, C., Sigl, M., Di  
711 Cosmo, N., Büntgen, U., 2018. The Eldgjá eruption: timing, long-range impacts and  
712 influence on the Christianisation of Iceland. *Clim. Change* 147, 369–381.  
713 <https://doi.org/10.1007/s10584-018-2171-9>



- 714 Papale, P., Moretti, R., Barbato, D., 2006. The compositional dependence of the saturation  
715 surface of H<sub>2</sub>O+ CO<sub>2</sub> fluids in silicate melts. *Chem. Geol.* 229, 78–95.  
716 <https://doi.org/10.1016/j.chemgeo.2006.01.013>
- 717 Patrick, M., Johanson, I., Shea, T., Waite, G., 2020. The historic events at Kīlauea Volcano in  
718 2018: summit collapse, rift zone eruption, and Mw 6.9 earthquake: preface to the special  
719 issue. *Bull. Volcanol.* 82, 46. <https://doi.org/0.1007/s00445-020-01377-5>
- 720 Pelleter, A.-A., Caroff, M., Cordier, C., Bachèlery, P., Nehlig, P., Debeuf, D., Arnaud, N., 2014.  
721 Melilite-bearing lavas in Mayotte (France): An insight into the mantle source below the  
722 Comores. *Lithos* 208, 281–297. <https://doi.org/10.1016/j.lithos.2014.09.012>
- 723 Perfit, M.R., Chadwick, W.W., 1998. Magmatism at mid-ocean ridges: Constraints from  
724 volcanological and geochemical investigations. *Geophys. Monogr. Geophys. Union* 106,  
725 59–116.
- 726 Petrone, C.M., Bugatti, G., Braschi, E., Tommasini, S., 2016. Pre-eruptive magmatic processes  
727 re-timed using a non-isothermal approach to magma chamber dynamics. *Nat. Commun.* 7,  
728 1–11. <https://doi.org/10.1038/ncomms12946>
- 729 Pouclet, A., Bellon, H., Bram, K., 2016. The Cenozoic volcanism in the Kivu rift: Assessment  
730 of the tectonic setting, geochemistry, and geochronology of the volcanic activity in the  
731 South-Kivu and Virunga regions. *J. African Earth Sci.* 121, 219–246.  
732 <https://doi.org/10.1016/j.jafrearsci.2016.05.026>
- 733 Putirka, K.D., 2008. Thermometers and Barometers for Volcanic Systems. *Rev. Mineral.*  
734 *Geochemistry* 69, 61–120. <https://doi.org/10.2138/rmg.2008.69.3>
- 735 Resing, J.A., Rubin, K.H., Embley, R.W., Lupton, J.E., Baker, E.T., Dziak, R.P., Baumberger,  
736 T., Lilley, M.D., Huber, J.A., Shank, T.M., 2011. Active submarine eruption of boninite  
737 in the northeastern Lau Basin. *Nat. Geosci.* 4, 799–806. <https://doi.org/10.1038/ngeo1275>
- 738 ReVoSiMa, 2021. Bulletin n°21 de l'activité sismo-volcanique à Mayotte, du 1 au 31 janvier  
739 2021. ISSN : 2680-1205. [https://www.brgm.fr/sites/default/files/documents/2021-  
740 02/dossier-thematique-mayotte-bulletin-revosima-026.pdf](https://www.brgm.fr/sites/default/files/documents/2021-02/dossier-thematique-mayotte-bulletin-revosima-026.pdf)
- 741 Roeder, P.L., Emslie, Rf., 1970. Olivine-liquid equilibrium. *Contrib. to Mineral. Petrol.* 29,  
742 275–289.
- 743 Rubin, K.H., Soule, S.A., Chadwick, W.W., Fornari, D.J., Clague, D.A., Embley, R.W., Baker,  
744 E.T., Perfit, M.R., Caress, D.W., Dziak, R.P., 2012. Volcanic eruptions in the deep sea.  
745 *Oceanography* 25, 142–157.
- 746 Saria, E., Calais, E., Stamps, D.S., Delvaux, D., Hartnady, C.J.H., 2014. Present-day kinematics  
747 of the East African Rift. *J. Geophys. Res. Solid Earth* 119, 3584–3600.  
748 <https://doi.org/10.1002/2013JB010901>
- 749 Sauerzapf, U., Lattard, D., Burchard, M., Engelmann, R., 2008. The Titanomagnetite - Ilmenite  
750 Equilibrium: New Experimental Data and Thermo-oxybarometric Application to the  
751 Crystallization of Basic to Intermediate Rocks. *J. Petrol.* 49, 1161–1185.  
752 <https://doi.org/10.1093/petrology/egn021>
- 753 Shea, T., Houghton, B.F., Gurioli, L., Cashman, K. V, Hammer, J.E., Hobden, B.J., 2010.  
754 Textural studies of vesicles in volcanic rocks: an integrated methodology. *J. Volcanol.*

755 Geotherm. Res. 190, 271–289. <https://doi.org/10.1016/j.jvolgeores.2009.12.003>

756 Späth, A., Roex, A.P. Le, Duncan, R.A., 1996. The geochemistry of lavas from the Comores  
757 Archipelago, Western Indian Ocean: petrogenesis and mantle source region  
758 characteristics. *J. Petrol.* 37, 961–991. <https://doi.org/10.1093/petrology/37.4.961>

759 Stamps, D.S., Saria, E., Kreemer, C., 2018. A Geodetic Strain Rate Model for the East African  
760 Rift System. *Sci. Rep.* 8, 732. <https://doi.org/10.1038/s41598-017-19097-w>

761 Strong, D.F., 1972. Petrology of the island of Moheli, western Indian Ocean. *Geol. Soc. Am.*  
762 *Bull.* 83, 389–406.

763 Thivet, S., Gurioli, L., Di Muro, A., 2020. Basaltic dyke eruptions at Piton de La Fournaise:  
764 characterization of the eruptive products with implications for reservoir conditions,  
765 conduit processes and eruptive dynamics. *Contrib. to Mineral. Petrol.* 175, 1–24.  
766 <https://doi.org/10.1007/s00410-020-1664-5>

767 Thompson, R.N., Flower, M.F.J., 1971. One-atmosphere melting and crystallization relations  
768 of lavas from Anjouan, Comores Archipelago, Western Indian Ocean. *Earth Planet. Sci.*  
769 *Lett.* 12, 97–107. [https://doi.org/10.1016/0012-821X\(71\)90060-4](https://doi.org/10.1016/0012-821X(71)90060-4)

770 Thordarson, T., Miller, D.J., Larsen, G., Self, S., Sigurdsson, H., 2001. New estimates of sulfur  
771 degassing and atmospheric mass-loading by the 934 AD Eldgjá eruption, Iceland. *J.*  
772 *Volcanol. Geotherm. Res.* 108, 33–54. [https://doi.org/10.1016/S0377-0273\(00\)00277-8](https://doi.org/10.1016/S0377-0273(00)00277-8)

773 Thordarson, T., Self, S., 1993. The Laki (Skaftár Fires) and Grímsvötn eruptions in 1783–1785.  
774 *Bull. Volcanol.* 55, 233–263. <https://doi.org/10.1007/BF00624353>

775 Tzevahirtzian, A., Zaragosi, S., Bachèlery, P., Biscara, L., Marchès, E., 2020. Submarine  
776 morphology of the Comoros volcanic archipelago. *Mar. Geol.* 432.  
777 <https://doi.org/10.1016/j.margeo.2020.106383>

778 Wadge, G., 1981. The variation of magma discharge during basaltic eruptions. *J. Volcanol.*  
779 *Geotherm. Res.* 11, 139–168. [https://doi.org/10.1016/0377-0273\(81\)90020-2](https://doi.org/10.1016/0377-0273(81)90020-2)

780 White, S.M., Crisp, J.A., Spera, F.J., 2006. Long-term volumetric eruption rates and magma  
781 budgets. *Geochemistry, Geophys. Geosystems* 7. <https://doi.org/10.1029/2005GC001002>

782 Zinke, J., Reijmer, J.J.G., Thomassin, B.A., Dullo, W.-C., Grootes, P.M., Erlenkeuser, H.,  
783 2003. Postglacial flooding history of Mayotte lagoon (Comoro archipelago, southwest  
784 Indian Ocean). *Mar. Geol.* 194, 181–196. [https://doi.org/10.1016/S0025-3227\(02\)00705-](https://doi.org/10.1016/S0025-3227(02)00705-3)  
785 3

786

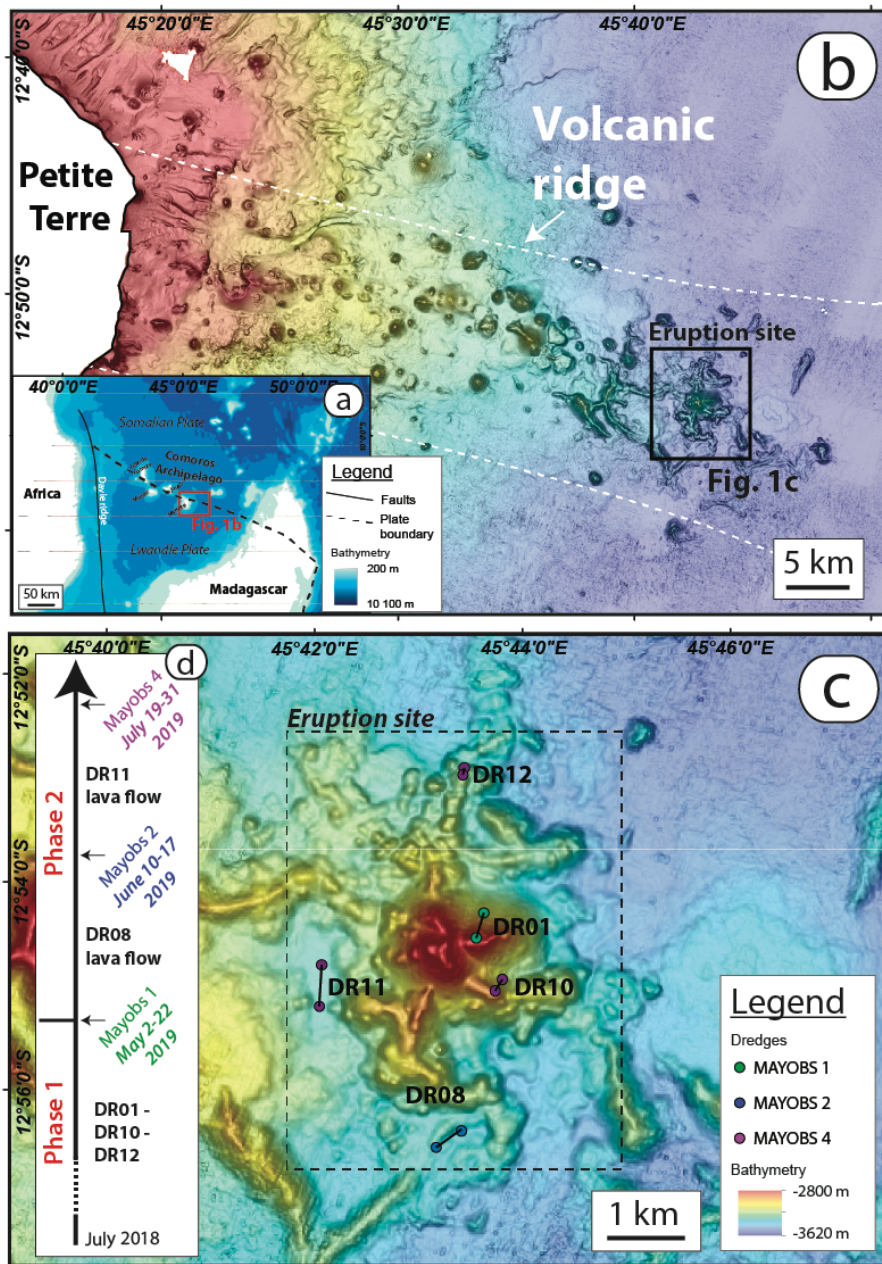
787

788

789

790

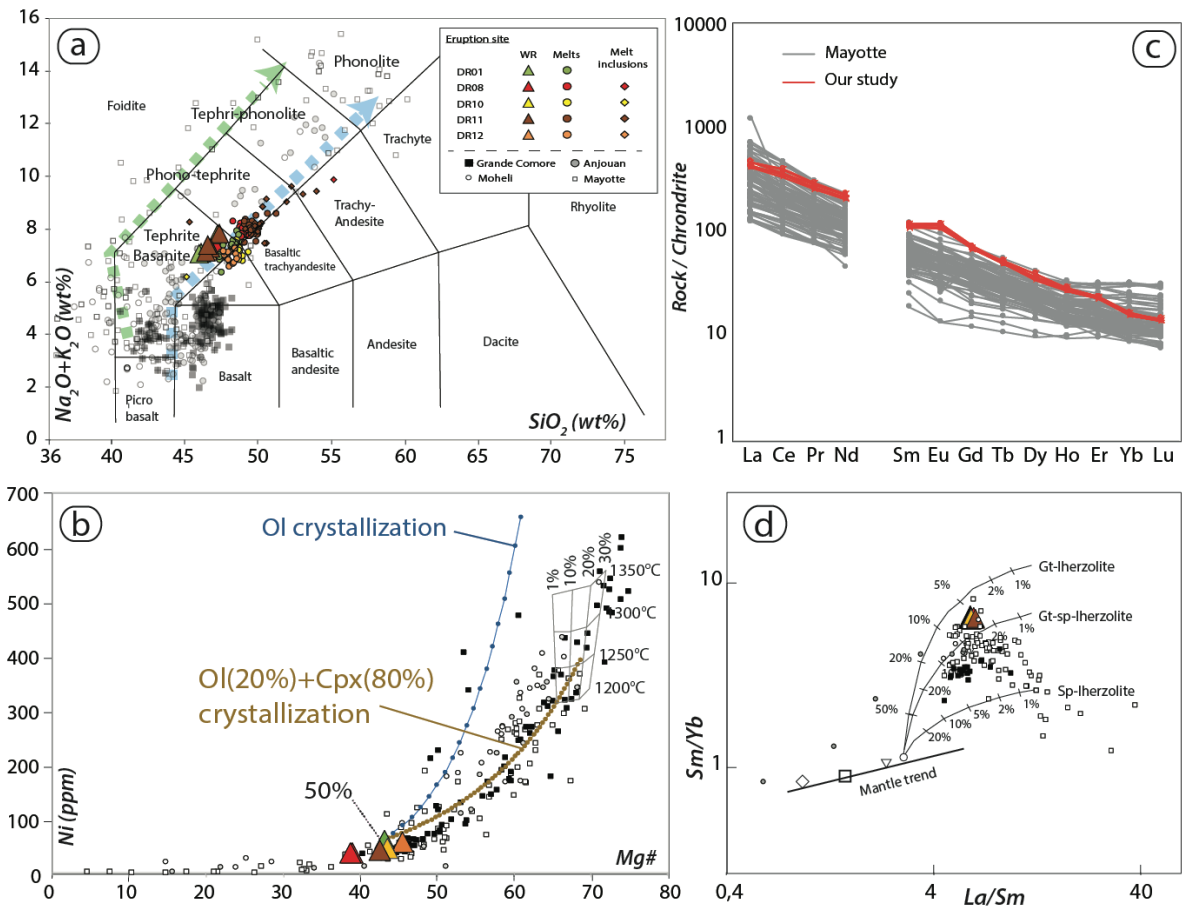
791



793

794 **Fig. 1:** Location of the eruptive site. a) Comoros volcanic archipelago is located in the northern  
 795 part of the Mozambique Channel. b) Location of the new volcanic edifice 50 km east of Mayotte  
 796 along the submarine volcanic ridge crossing Mayotte eastern flank. c) Location of the five  
 797 dredges (DR) carried out during the three oceanographic campaigns (MAYOBS 1, 2 and 4),  
 798 superimposed on bathymetric data from the MAYOBS 1 cruise (May 2019). d) Sampling  
 799 related to eruption timing. DR01, DR10 and DR12 lavas were erupted before May 2019 during

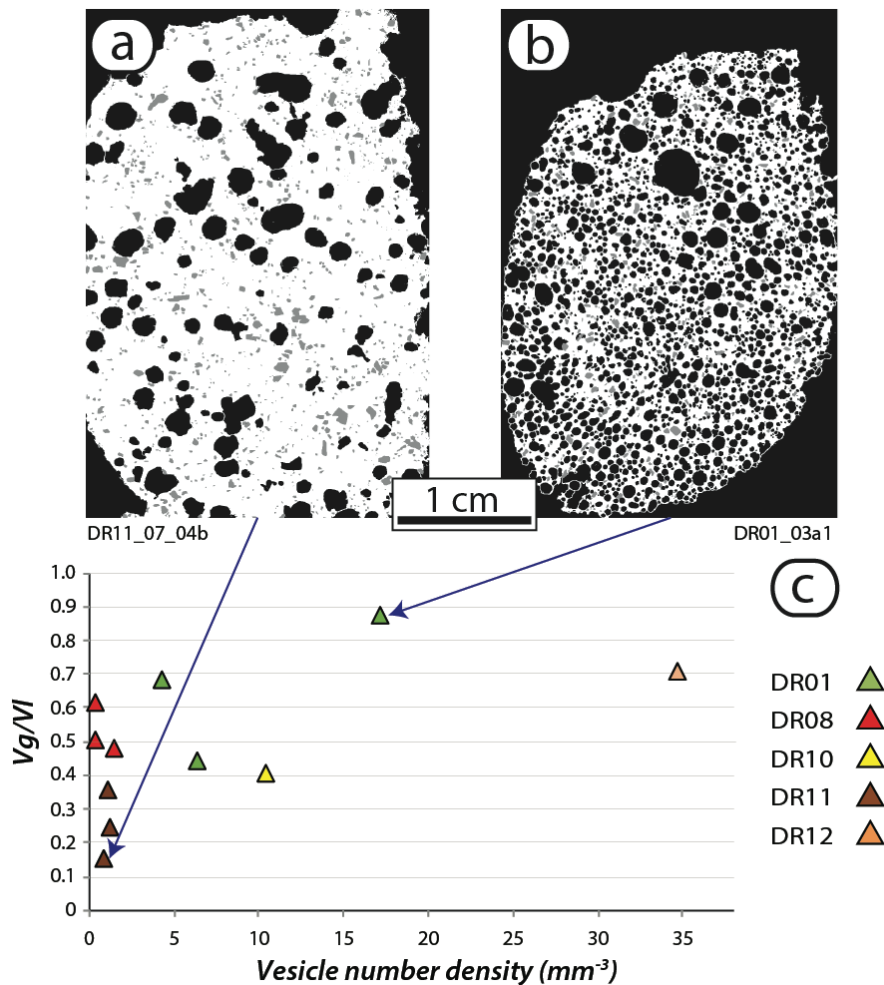
800 the cone-building phase 1 and sampled by MAYOBS 1 and 4 oceanographic cruises; DR08 and  
 801 DR11 are lava flows emitted in June and July 2019 (phase 2) and sampled during Mayobs 2  
 802 and 4 oceanographic cruises, respectively.



803

804 **Fig. 2:** Bulk rock geochemistry of the dredged evolved basanite lavas emitted during the 2018-  
 805 2020 Mayotte eruption. a) TAS classification comparing the composition of the submarine  
 806 lavas of the new edifice (Suppl. material Table 1) with that of subaerial lavas from the Comoros  
 807 archipelago. Blue and green arrows show the moderately silica-undersaturated (“Karthala-  
 808 trend”) and the highly silica-undersaturated (“La Grille-trend”) trends identified in Comoros  
 809 lavas, respectively. b) Fractional crystallization models for Comoros and Mayotte lavas plotted  
 810 in Ni (ppm) vs  $\text{Mg}\#$  space. Melts in equilibrium with the mantle have a  $\text{Mg}\# \sim 70$  (the melting  
 811 grid with mantle melting temperature and melt fractions has been computed following Späth et  
 812 al., 1996)). Back calculation models start from DR0101 composition by adding in small

813 increments of equilibrium olivine and clinopyroxene compositions appropriate to match the  
 814 composition of subaerial Comoros lavas and consistent with the Ni concentration for a primary  
 815 mantle melt (300-500 ppm, Späth et al., (1996)). Olivine-only fractionation fails to reproduce  
 816 the Comoros trend. c) Chondrite-normalized REE patterns of the submarine lavas of the new  
 817 edifice compared to Mayotte subaerial lavas. d) La/Sm vs Sm/Yb diagram annotated with  
 818 partial melting curves for garnet and spinel lherzolite mantle sources (Pouclet et al., 2016).

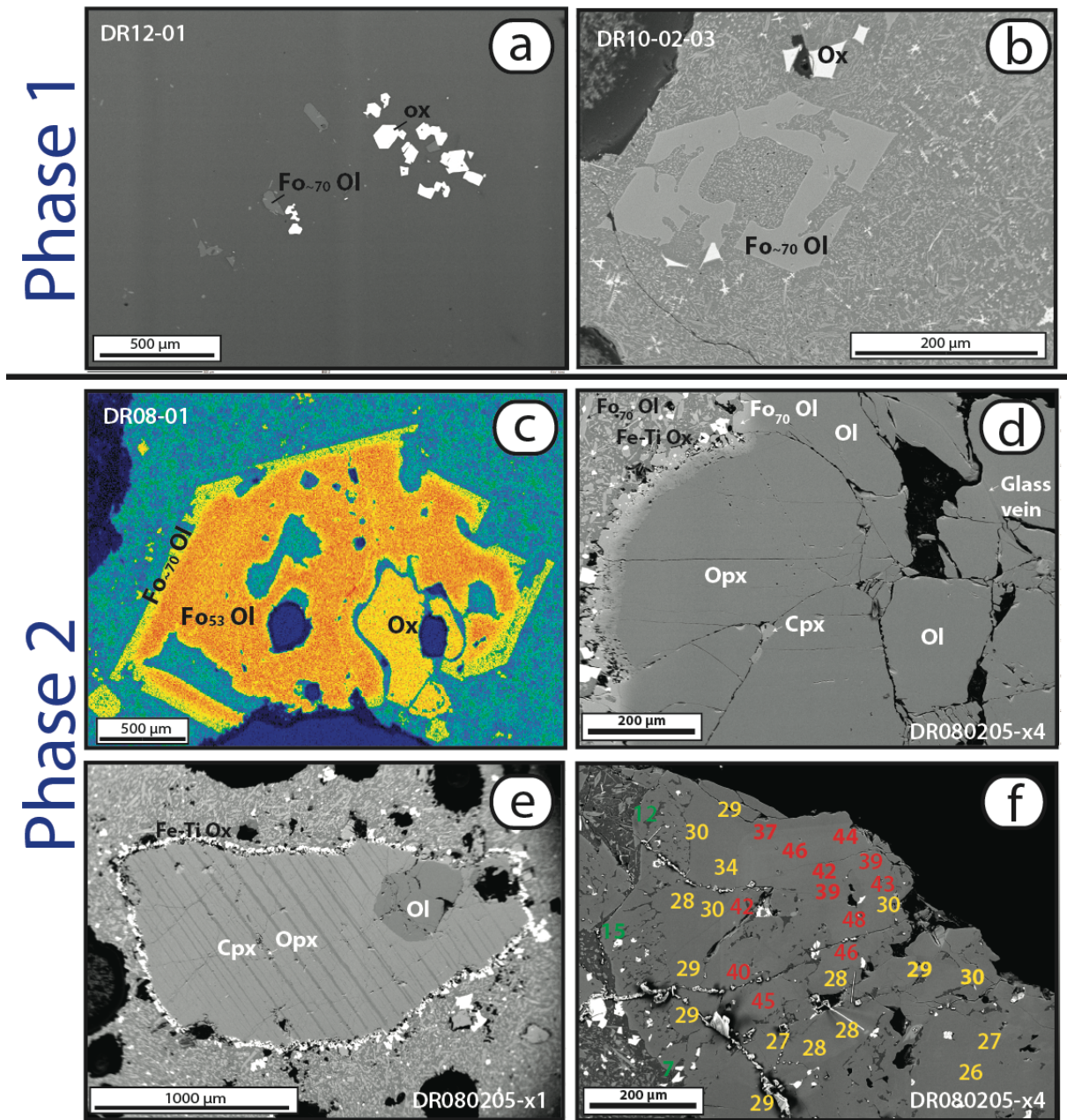


819

820 **Fig. 3:** Textural characteristics of the studied lava samples. Binary images of two lava  
 821 fragments a) DR110704-b and b) DR0103-a1 where black = vesicles, white = glass and grey =  
 822 crystals. c) Vesicle to melt ratio (Vg/Vl) vs. vesicle number density. A decrease in vesicle  
 823 number density (Nv) is evident from the samples from phase 1 (DR01-DR10-DR12) to those



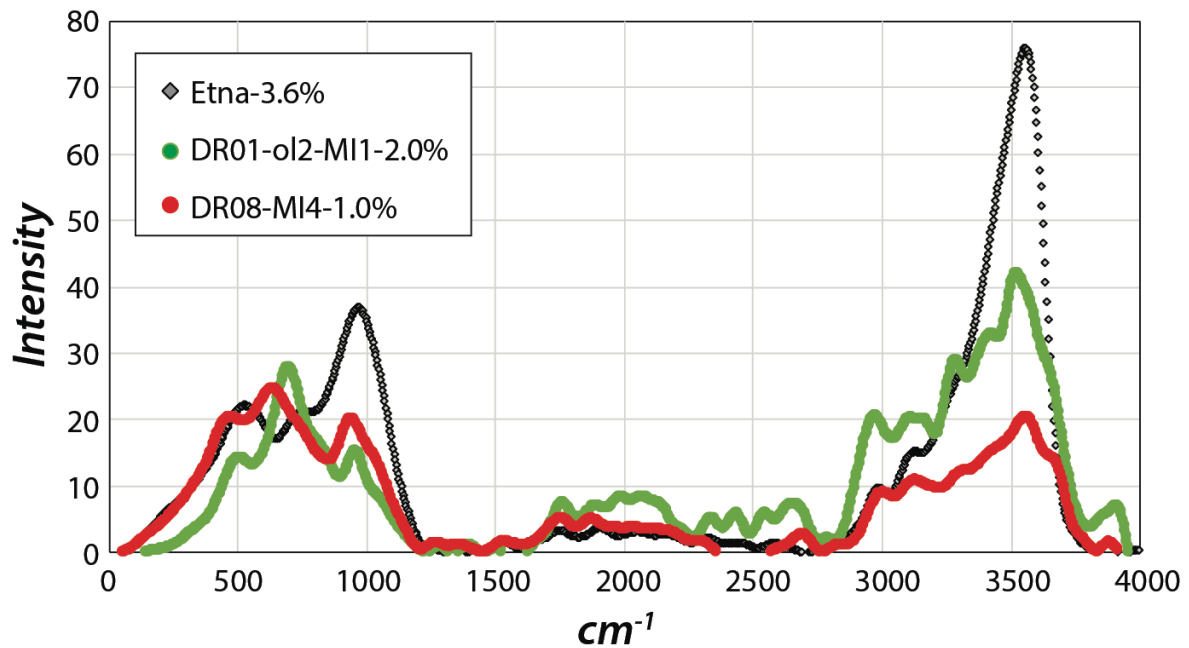
824 from phase 2 (DR08-DR11), with DR11 samples being the lowest in term of vesicularity and  
 825 inferred pre-eruptive gas content.



826

827 **Fig. 4.** Petrographic features of the dredged lavas. a) All lavas have very low crystallinity: BSE  
 828 image of 4 – 6% microlites of Fo<sub>~70</sub> olivine (Fo<sub>~70</sub> Ol, Suppl. material Table 4) and  
 829 titanomagnetite (Ox) in glassy matrix of sample DR1201. b) Many crystals show textures  
 830 typical of fast growth like these skeletal Fo<sub>70</sub> olivine and titanomagnetite crystals in fine-grained  
 831 groundmass (sample DR100203) c) Olivine crystals in late erupted lavas (DR08; DR11) have

832 low-Fo composition (Fo<sub>53</sub>) and show reverse zoning (MnO element map); these crystals are  
 833 associated with large titanomagnetite crystals (ox). d) Harzburgite mantle xenolith from the  
 834 later erupted lavas (sample DR080205-x4) composed of Fo<sub>90</sub> olivine and Mg#<sub>90</sub> orthopyroxene  
 835 (Opx); Mg#<sub>90-93</sub> clinopyroxenes (Cpx) are associated with SiO<sub>2</sub> and K<sub>2</sub>O-rich veins. e) Another  
 836 mantle xenolith composed of a single crystal of Cpx with Opx exsolutions (sample DR080205-  
 837 x1) and a few olivine and Opx crystals. f) Zoned clinopyroxene megacryst in sample  
 838 DR080205-x2. Superimposed colored numbers show estimated depth of crystallization  
 839 calculated through geobarometry (Putirka, 2008): red numbers are located in the low- Mg#  
 840 core, yellow: high-Mg# inner rim, green: dendritic outer rim.



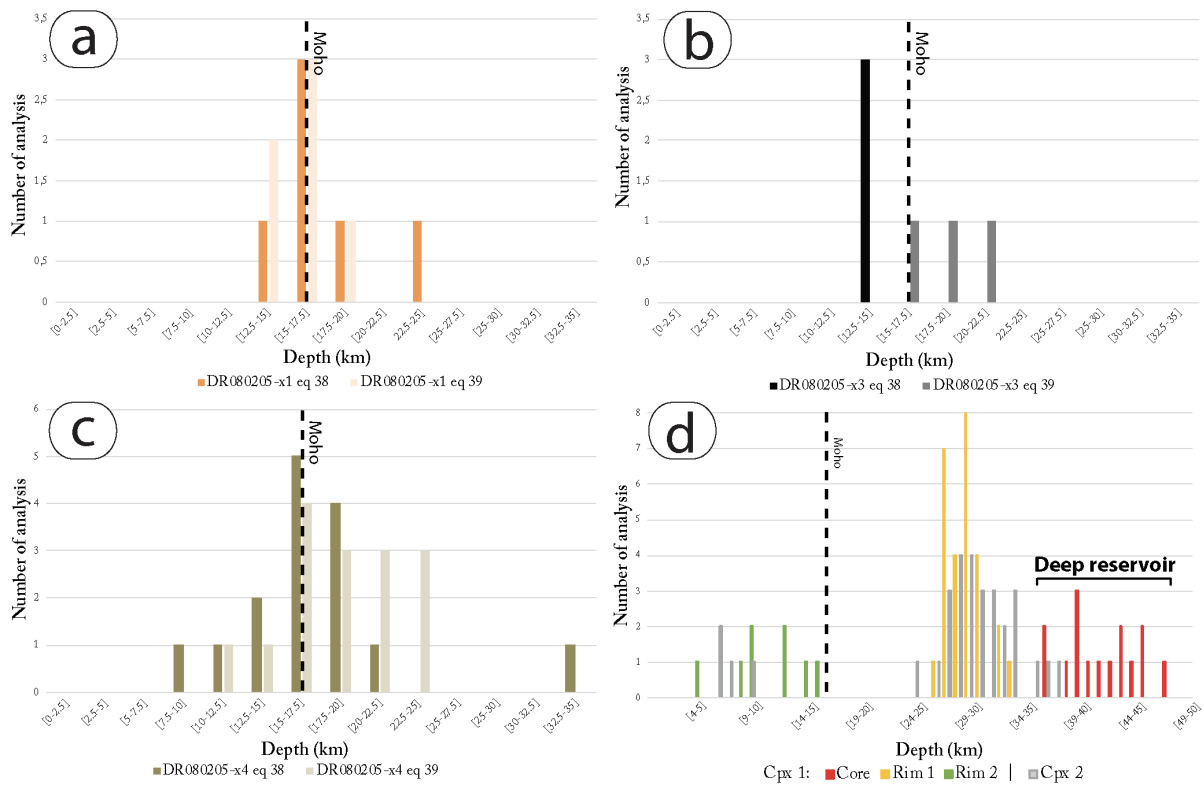
ID	DR1-03-ol2-FI1	DR1-03-ol2-MI1	DR1-03-ol3-emb	DR1-03-ol4-MI	DR8-01-MI1	DR8-01-MI2	DR8-01-MI3	DR8-01-MI4
Glass	melt inclusion	melt inclusion	embayment	melt inclusion	melt inclusion	melt inclusion	melt inclusion	melt inclusion
Host	olivine	olivine	olivine	olivine	spinel	spinel	spinel	spinel
H <sub>2</sub> O	2.0	0.6	2.2	2.3	1.2	1.0	1.1	1.0

841

842 **Fig. 5** Raman spectra of an olivine-hosted melt inclusion from sample DR0103 and a spinel-  
 843 hosted melt inclusion from sample DR0801 compared with reference basaltic glass containing  
 844 3.6 wt% of dissolved water (Etna glass). Bands in the 100-1200 cm<sup>-1</sup> region are related to  
 845 vibrations of the glass network, while the band at 3570 cm<sup>-1</sup> is produced by stretching of OH

846 bonds and its intensity linearly correlates with the concentration in total dissolved water (Di  
 847 Muro et al., 2006). Table shows H<sub>2</sub>O content (wt%) in melt inclusions and embayment in  
 848 DR0103 and DR0801 samples.

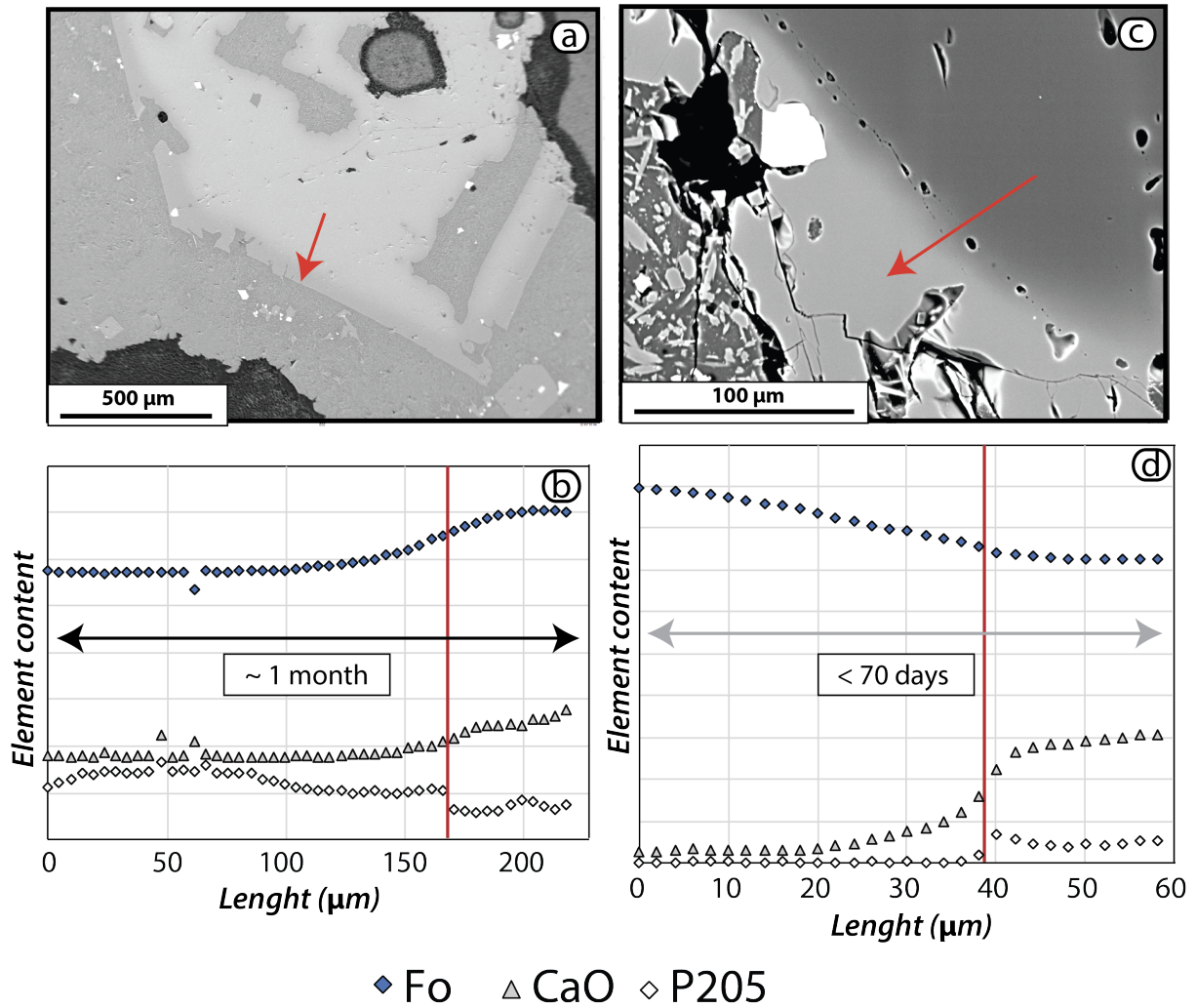
849



850

851 **Fig. 6:** Histograms showing depth obtained using geobarometry on clinopyroxene-  
 852 orthopyroxene pairs in the mantle xenoliths in the June 2019 lava flow (DR08). The different  
 853 colored bars represent results from using different equations (see discussion in text). Pyroxenes  
 854 located in the three mantle xenoliths (Fig. 4d, e) were equilibrated at pressures of  $0.43 \pm 0.19$   
 855 GPa, near the depth of the Moho at 15 – 18 km (black dashed line). (a) DR080205-x1,  $0.41 \pm$   
 856  $0.19$  GPa, (b) DR080205-x3 and  $0.46 \pm 0.19$  GPa (c) DR080205-x4; d) We obtained two  
 857 additional clusters of pressures of 1.01 – 1.34 GPa and 0.62 – 0.92 GPa with a second set of  
 858 geobarometry estimations using zoned clinopyroxene megacrysts (Fig. 4f). Moho is shown by  
 859 a black dotted line (Dofal et al., 2018).





861

862 **Fig. 7:** Core-rim diffusion profiles in zoned olivines. Red arrows show the trace of the profiles

863 on BSE images of a) a reversely-zoned olivine in the DR0801b ALF sample, and c) a normally

864 zoned olivine in the xenolith from the DR080205x4 sample. b) and d) shows Fo, CaO and P<sub>2</sub>O<sub>5</sub>

865 core-rim profiles corresponding to the traces presented in a) and c) (Suppl. material Table 6).

866 The diffusion rate for P in olivine is extremely slow so this immobile element marks the initial

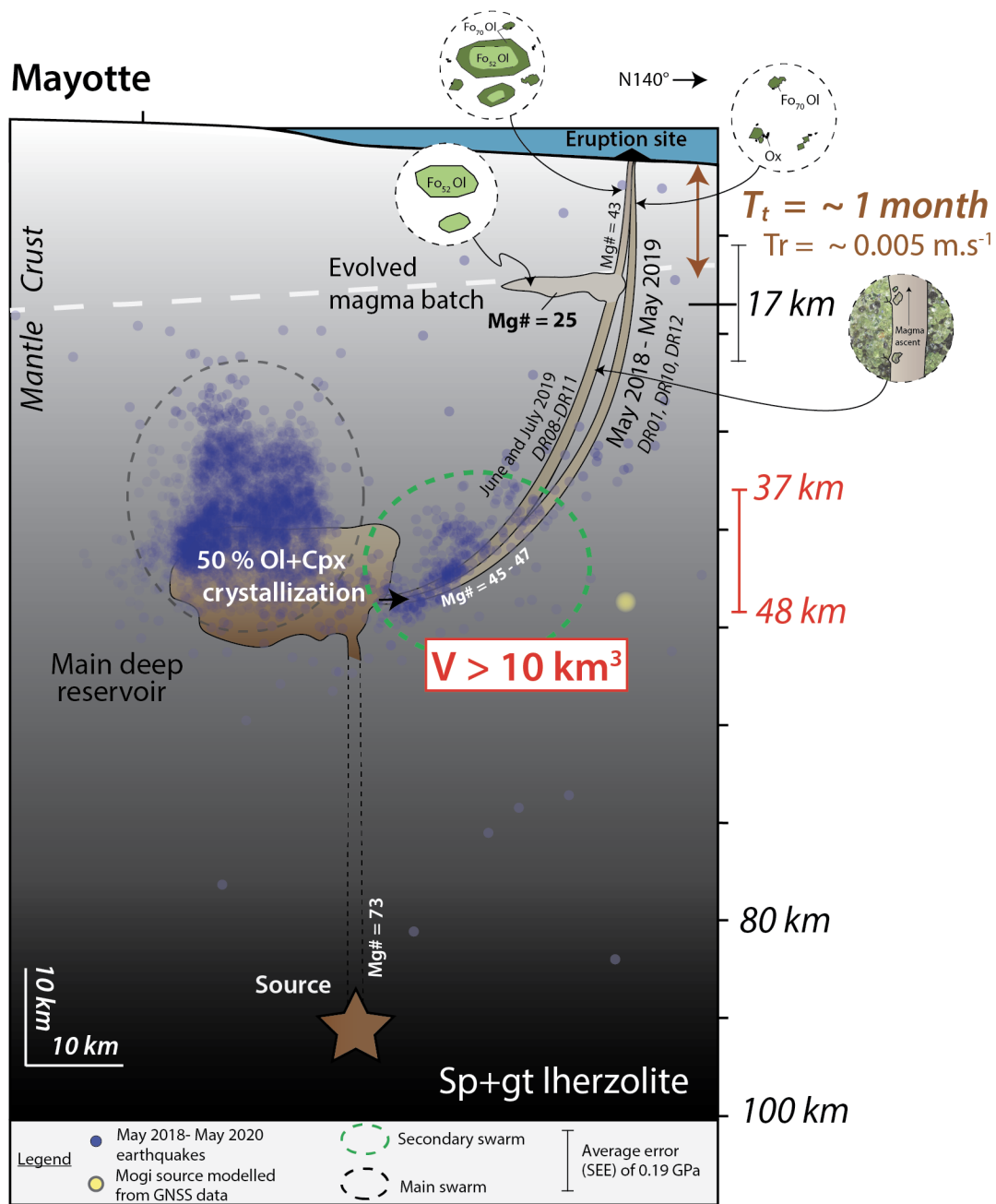
867 boundaries between zones that crystallized at different times. In the reversely-zoned phenocryst

868 of b), the initial profile was a step between a Fo<sub>53</sub> core and a Fo<sub>70</sub> rim, then Ca and Mg/Fe

869 diffused away from this initial step. In the normally zoned xenolith of d), the initial profile was

870 a step between a Fo<sub>90</sub> core and a Fo<sub>72</sub> rim, then Ca and Mg/Fe diffused away from this initial

871 step.



873

874 **Fig. 8.** Magma plumbing system feeding the 2018-2020 Mayotte eruption interpreted on the  
 875 basis of petrological and geophysical data. Magma produced by partial melting of a spinel (sp)  
 876 + garnet (gt) lherzolite mantle source undergoes 50% of crystallization (80% cpx + 20% ol) in  
 877 a large and  $\geq 37$  km deep magma reservoir with a volume  $\geq 10$  km<sup>3</sup>. Depth of this main deep  
 878 storage unit constrained by barometric data is in excellent agreement with seismicity location  
 879 (blue dots, ReVoSiMa, 2021) and geodetic model (yellow dot). Starting from the main deep

880 reservoir, the magma path evolved during the eruption. During the first year, eruption is fed by  
 881 direct ascent of magma from the deep reservoir to the surface through NW-SE lithospheric  
 882 structures. The shape and the size of microlites indicate that most micro-crystallization occurred  
 883 in the shallow part of the ascending dyke. A shallower and smaller differentiated magma  
 884 reservoir located close to the Moho ( $< 17 \pm 6$  km) was sampled *en route* during the second year  
 885 of the eruption. It is important to note that this magma batch and the shallow conduit were not  
 886 imaged by on-land seismometers because they are located too far from the eruption site to allow  
 887 identification of small, shallow earthquakes. Moho: grey dotted line (Dofal et al., 2018). Tt:  
 888 Transfer time, Tr: Transfer rate = distance / transfer time, V: volume.

889

890 **Table captions**

891

Dredges	Oceanographic cruise	DOI : 10.18142/291	Start dredging			End dredging		
			Latitude	Longitude	Depth	Latitude	Longitude	Depth
DR01	MAYOBS 1	10.17600/18001217	12°54.30' S	45°43.13' E	3050 m	12°54.51' S	45°43.08' E	2820 m
DR08	MAYOBS 2	10.17600/18001222	12°56.46' S	45°42.88' E	3072 m	12°56.05' S	45°41.91' E	3050 m
DR10	MAYOBS 4	10.17600/18001238	12° 54.94' S	45° 43.31' E	3120 m	12° 55.05' S	45°43.24' E	2950 m
DR11	MAYOBS 4	10.17600/18001238	12°54.80' S	45°41.57' E	3250 m	12°55.20' S	45°41.55' E	3228 m
DR12	MAYOBS 4	10.17600/18001238	12°52.90' S	45°42.94' E	3245 m	12°52.97' S	45°42.93' E	3200 m

892

893 **Tab. 1:** Location of dredges performed during MAYOBS 1 (DR01), MAYOBS 2 (DR08) and  
 894 MAYOBS 4 (DR10, DR11 and DR12) oceanographic campaigns. No dredges were performed  
 895 during MAYOBS 3.

896

897